Supplementary Information (SI) for

"ADAM-10 and -17 regulate endometriotic cell migration via concerted ligand and receptor shedding feedback on kinase signaling"

Miles A. Miller[1,2†], Aaron S. Meyer[1,2†], Michael Beste[1,2], and Zainab Lasisi[1,2], Sonika Reddy[1,2], Karen Jeng[1,2], Chia-Hung Chen[3,4], Jongyoon Han[1,3], Keith Isaacson[2,5] Linda G. Griffith[1,2] Douglas A. Lauffenburger[1,2*]

1 Department of Biological Engineering, Massachusetts Institute of Technology, Cambridge, MA 02139, USA
2 Center for Gynepathology, Massachusetts Institute of Technology, Cambridge, MA 02139, USA
3 Department of Electrical Engineering and Computer Science, Massachusetts Institute of Technology, Cambridge, MA 02139, USA
4 Department of Biological Engineering, National University of Singapore, Singapore 117576
5 Newton-Wellesley Hospital, Harvard Medical School, Newton, MA 02462
† equal contribution ∗ E-mail: lauffen@mit.edu

Contents

1 Table of key proteins and their clinical association with endometriosis.

Nearly all growth factors, kinases, cytokines, RTKs, ligands, and proteases directly measured in this work have been implicated in endometriosis by previously reported clinical data. TNFa = tumor necrosis factor alpha; Erk1/2 = extracellular related kinase 1/2; Jnk = c-Jun N-terminal kinase; HSP27 = heat-shock protein 27; STAT3 = signal transducer and activator of transcription 3; IRS-1 = insulin receptor substrate 1; Tyk2 = tyrosine kinase 2; PGE = prostaglandin E.

Protein	Disease Trend	Evidence	Citations	Notes
Environmental Stimuli				
TNFα	Up/Unchanged	S/PF/A	[1–5]	
EGF	Up/Unchanged	PF/A	[6–8]	
TGFα	Up	A	[8]	
NRG1β	Up*		[9]	*Ovarian cancer
PDGFbb	Unchanged	S/PF	[3, 10]	
HGF	Up	PF	[11]	
IGF1	Up/Unchanged	S	[12–14]	
Intracellular Phospho-Signaling Proteins				
p-p38	Up	T/A	[15–17]	
p-Erk1/2	Up*	T	[18, 19]	*Total protein unchanged
p-Jnk	Up*	T/A	[20, 21]	*Endometriotic endothelium
HSP27	Up	T	[22, 23]	Total protein increased
c-Jun	Up*	T	[24, 25]	*RNA expression increased
p-Akt	Up	T	[19, 26, 27]	Both p-Akt and tot. Akt increased
p-STAT3	Up	T	[28]	
Src	N/A*	T	[29, 30]	*Assoc. *in vitro* w/ MMP & PGE
IRS-2	N/A	GP	[31]	Pos. assoc. with disease
Tyk2	N/A	GP	[32]	Assoc. with decreased risk
Receptors and Autocrine Ligands				
EGFR	Unchanged*/Up**	T/S	[12, 33, 34]	*Up w/ danazol; **Eutopic
TNFR1	Up	S/PF	[13, 35]	
MET	Up*	T	[36]	*Cell surface expression
HER-2	Up*/Unchanged	T/S	[34, 37, 38]	*Up in endometriosis-assoc. cancer
AREG	Up	T	[39]	
HBEGF	Up	T	[39]	
MMPs and TIMPs				
MMP-2	Up	T/S/PF	[40, 41]	
MMP-3	Up	A/T	[42–44]	
MMP-7	Up	A/GP	[43, 45]	
MMP-9	Up	T/PF	[46–48]	
TIMP-1	Up/Down	T/S/PF	[42, 48–50]	
TIMP-2	Down	T	[40, 50]	
ADAMs				
ADAM-17	Up	T	[50]	
ADAM-10	Up	T	[51]	

S = serum, PF = peritoneal fluid, T = tissue, GP = genetic polymorphism, A = animal model

2 CSR data: phospho-protein response to growth factor stimulation.

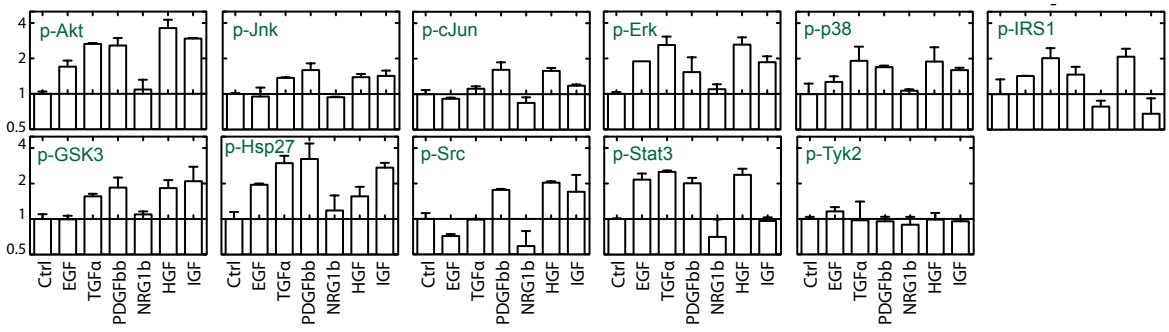

Data shown here were incorporated directly in CSR dataset (Figs. 1B-C). Phospho-proteins were quantified from cells lysed 5 min. post-stimulation, also shown in Fig. 2A (n=2 biological reps.). All error bars denote S.E.

3 CSR data: sheddase activity using FRET-substrate, PrAMA inference, and IP+activity assays.

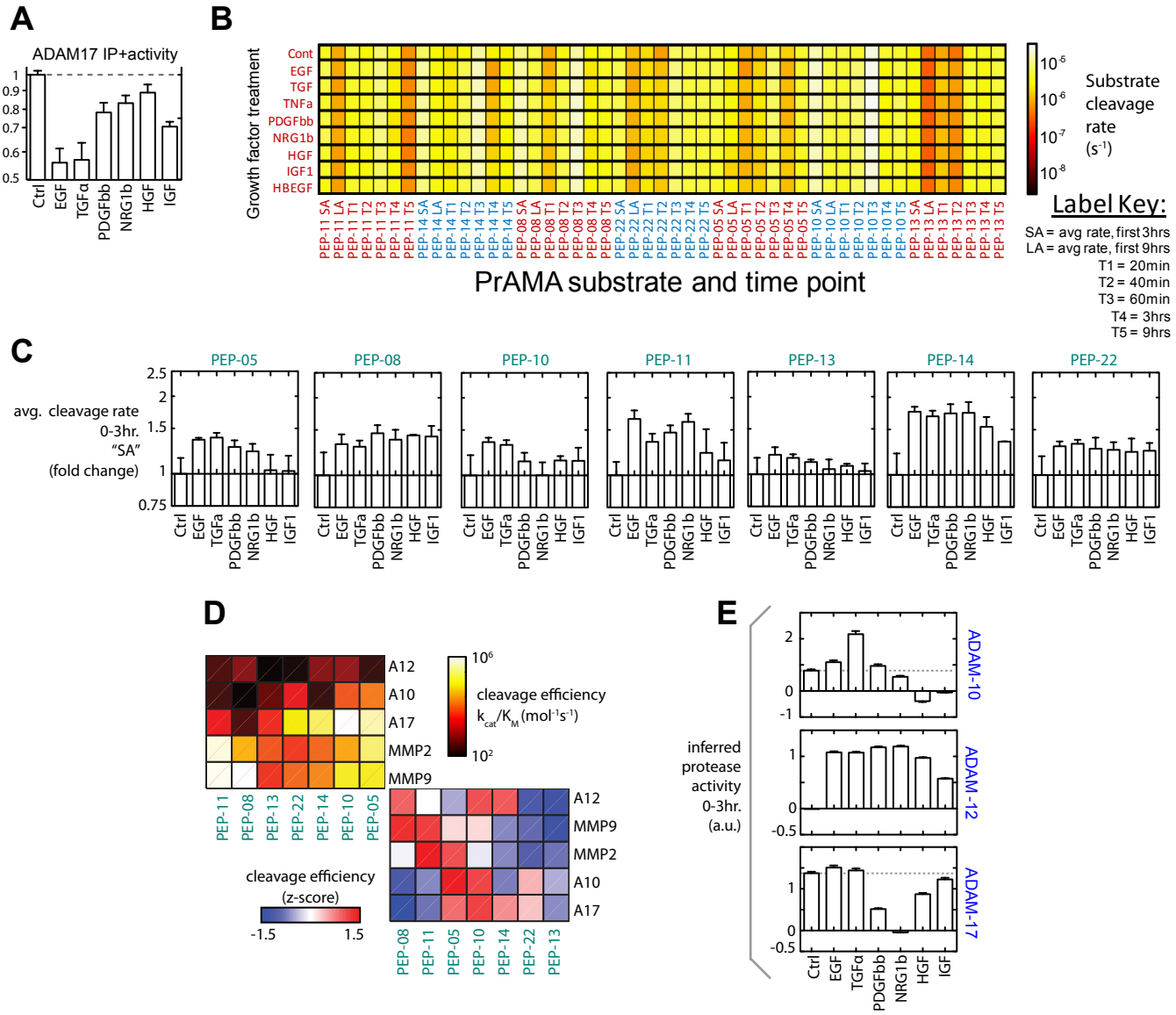

A subset of the data shown here was incorporated directly in the CSR dataset (Figs. 1B-C, 2A). **(A)** ADAM17 activity was quantified using the Innozyme TACE activity assay (see SI-19 for protocol) from whole-cell lysate collected 45 min. post-stimulation (also shown in Fig. 2A; n=2 biological reps.). **(B)** Seven soluble, FRET-based synthetic polypeptide protease substrates were added concomitantly with growth factors to serum-starved 12Z cultures. Fluorescence was recorded at five time points, and cleavage kinetics were calculated from the rate of fluorescence increase for each substrate and growth factor condition (n=4 biological reps.). The heat-map shows the cleavage rates for each time interval, as well as average kinetics across the first three hours ("SA") and across the first nine hours ("LA"). **(C)** Only the "SA" data were used in the integrative cue-signal-response modeling (Fig. 2A), and comprise the average of n=4 biological reps. across 5 time-point readings. **(D)** Hierarchical biclustering of catalytic efficiencies for the panel of FRET-substrates used in *B-C*. Enzymatic efficiencies were previously reported [52], measured using purified recombinant enzymes. The top-left heat-map shows absolute catalytic efficiencies. The bottom-right heat-map shows efficiencies after each row has been mean-centered and variance-normalized, and consequently shows relative substrate efficiencies for each enzyme. Of note, PEP-05 exhibits peptide sequence similar to pro-TNFa, and known ADAM substrate, and PEP-10 is closely related. PEP-13 shares sequence similarity with the known ADAM10 substrate, CD23. **(E)** PrAMA was used to infer specific ADAM activities from the FRET-substrate cleavage measurements shown in *C* (n=4 reps.; data also shown in Fig. 2A). PrAMA algorithm parameters have been previously described [53]. All error bars indicate S.E.

4 CSR data: ADAM-10 and -17 surface levels, ADAM-17-pT735, and ADAM-17 dimers.

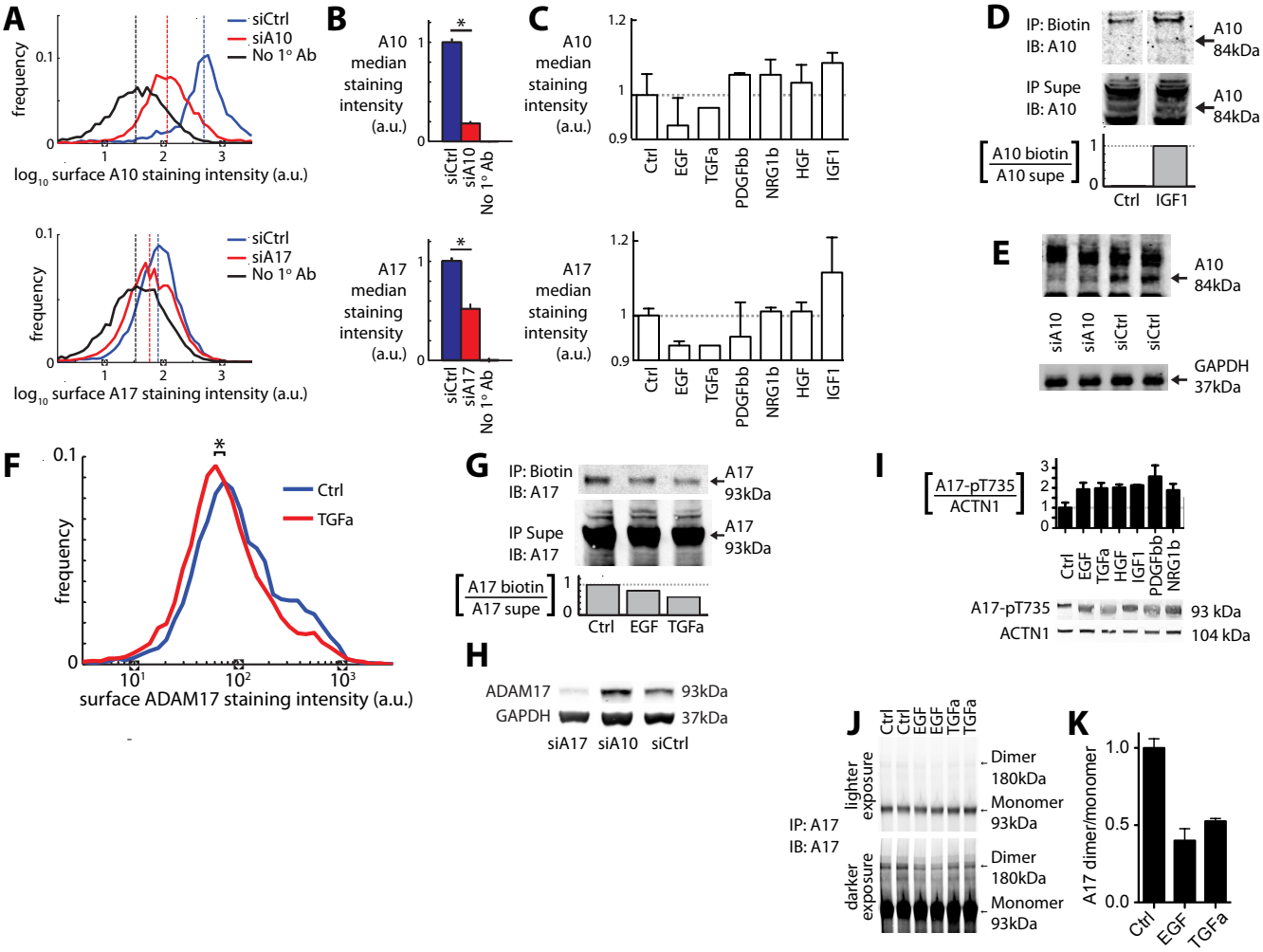

Data shown here were either incorporated directly in the CSR dataset (Figs. 1B-C, 2A), or validate those incorporated measurements. **(A-B)** siRNA experiments confirm Ab specificity for ADAM-10 and -17 (see SI-19 for siRNA protocols). Live-cell immunostaining and cytometric analysis show single-cell population distributions of staining intensities (A) and their corresponding averages (B), confirming Ab specificity ($^*p<0.05$). Staining in the absence of a primary Ab treatment but after secondary Ab treatment ("No 1^o Ab") was used to determine background signals. **(C)** Staining was performed as in *A-B*, but following growth-factor stimulation. Cells were stained 30 min. post-stimulation (also shown in Fig. 2A; n=3 reps.). **(D)** Western blot confirms IGF1 upregulates surface ADAM10. 30 min. post-IGF1 stimulation, cells were treated with sulfo-NHS-biotin, lysed, and incubated with streptavidin beads (see SI-19 for protocol). Bound and unbound proteins ("IP:Biotin" and "IP Supe", respectively) were then blotted for ADAM10. The bar-plot shows surface ADAM10 quantified by densitometry. **(E)** Using the same Ab as in *D*, western blots of lysates from siRNA-treated cells confirm the 84 kDa band corresponds to ADAM10, exhibiting significantly decreased band intensity upon knockdown (n=2 reps., $p<0.05$). **(F)** Population distribution of single-cell staining intensity for ADAM17 (measured by cytometry), following treatment with TGFa. Results correspond to the bar-plot in *C* ($^*p<0.05$, n=3 reps.). **(G)** Western blot confirms EGF and TGFa downregulate surface ADAM17. 30 min. post-stimulation, cells were treated with sulfo-NHS-biotin, lysed, and incubated with streptavidin beads (see SI-19 for protocol). Bound and unbound proteins ("IP:Biotin" and "IP Supe", respectively) were then blotted for ADAM17. **(H)** Using the same Ab as in *G*, western-blots of lysates from siRNA-treated cells confirm the 93 kDa band corresponds to ADAM17, exhibiting signficantly reduced band intensity upon knockdown (n=2 reps., $p<0.05$). **(I)** Representative blots showing ADAM17-pT735, and ACTN1-normalized quantitation by densitometry (also shown in Fig. 2A; n=3 biological reps.). Measurements were taken from whole-cell lysates 30 min. post-stimulation. **(J)** ADAM17 dimerization decreases following EGF and TGFa treatment. 30 min. post-stimulation, cells were treated with sulfo-EGS and lysed. Immunoprecipitated ADAM17 from lysates was blotted for ADAM17. **(K)** The ratio of dimer to monomer band intensity was calculated using quantification by densitometry. All error bars denote S.E., $^*p < 0.05$, Student's t-test.

5 CSR data: Myc-HBEGF shedding assay, validation, and results.

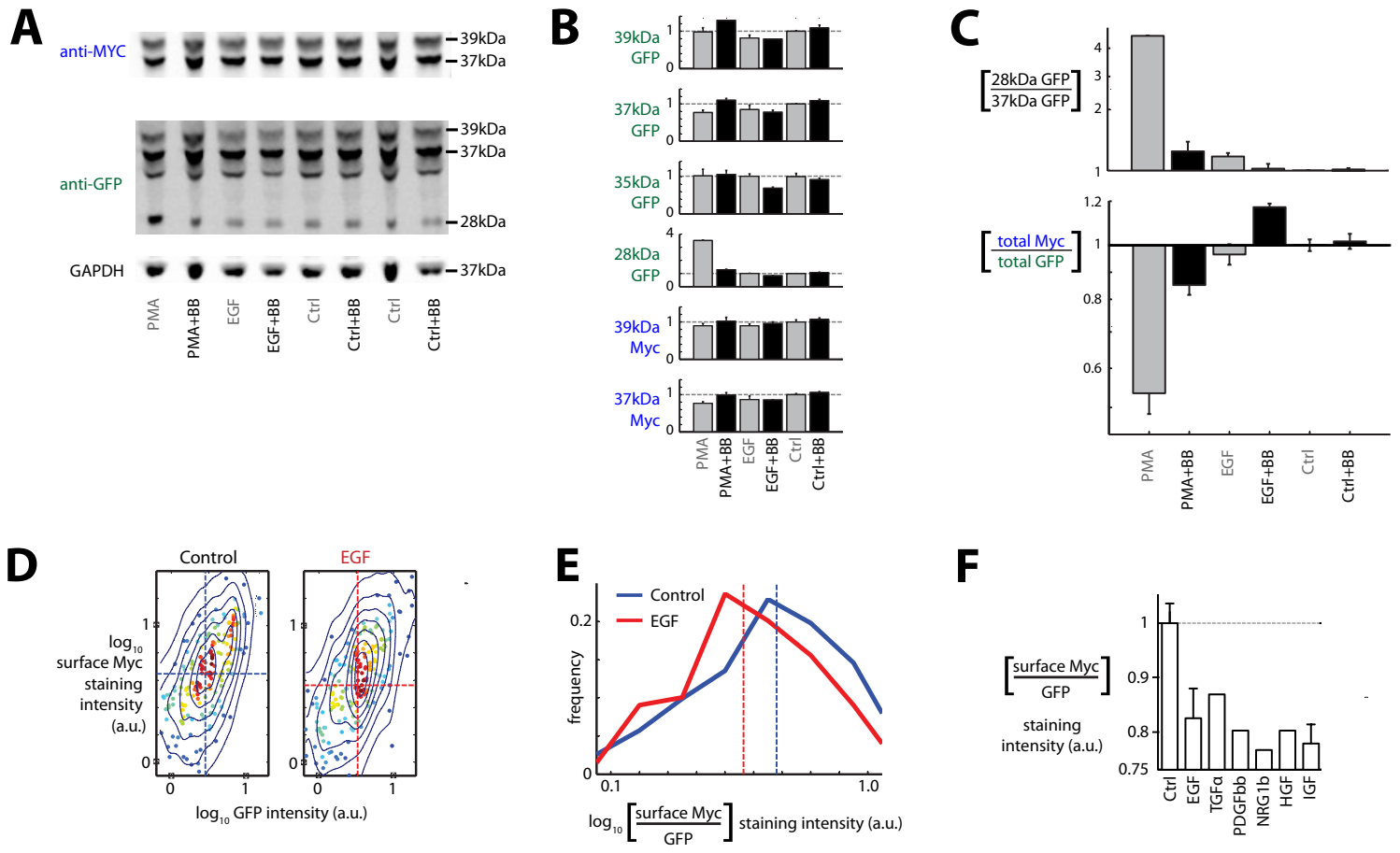

Data shown here were either incorporated directly in the CSR dataset (Figs. 1B-C, 2A), or validate those incorporated measurements. Because HBEGF is expressed at a low level in 12Z, we transgenically over-expressed the protein in 12Z to directly measure its shedding at short time-points following growth factor stimulation. We used a retroviral construct with a GFP-tagged intracellular c-terminus and a Myc-tagged ectodomain, as described previously [54]. **(A)** Representative western blots demonstrate modest yet statistically significant HBEGF shedding in response to 1uM phorbol ester (PMA) and EGF stimulation, in a BB94-dependent manner. As expected based on original description of the construct [54], full-length HBEGF protein products can be detected at 39, 37, and 35 kDa by the anti-GFP Ab. The primary ADAM-mediated cleavage product is visible at 28 kDa. Also consistent with the previous study, the 37 kDa fragment is most prominent for anti-Myc staining, followed by the 39 kDa fragment. At the relatively lower expression levels here compared to the previous implementation [54], the 35kDa fragment was undetectable by anti-Myc staining. **(B)** Band intensities from *A* and another replicate were quantified by densitometry and normalized to GAPDH measurements. **(C)** Top: The ratio of primary HBEGF cleavage product (28 kDa) and primary full-length protein (37 kDa) was calculated from *B*. Results indicate PMA and EGF significantly increase the ratio in a BB94-dependent manner. Bottom: To generate numerical values that would be reflective of cell-surface immunostaining and flow-cytometry experiments, the ratio of total Myc to total GFP staining intensity was calculated. Total Myc staining was calculated by summing band intensities at 37 kDa and 39 kDa. Total GFP staining was calculated by summing band intensities at 28 kDa, 35 kDa, 37 kDa, and 39 kDa. Results indicate PMA decreases the ratio in a BB94-dependent manner. **(D)** Single-cell flow-cytometry scatterplots showing GFP intesity vs. surface Myc staining intensity, 30 min. following EGF stimulation. Each point represents a single-cell measurement, with warmer colors indicating higher point-density. Contour lines indicate population distribution, and dotted lines denote median intensity values. **(E)** Single-cell population distribution of the ratio in Myc and GFP intensities, corresponding to data in *D*. Dotted lines indicate population medians. **(F)** Results from *D-E*, along with measurements from the other growth-factor treatment conditions, averaged over n=9 total replicates (also shown in Fig. 2A). Data represent the control-normalized averages of measurements taken at 30, 60, and 90 min. post-stimulation (n=3 reps. x 3 time-points per growth-factor condition). All error bars denote S.E.

6 CSR data: endogenous ligand/receptor ectodomain surface and supernatant levels.

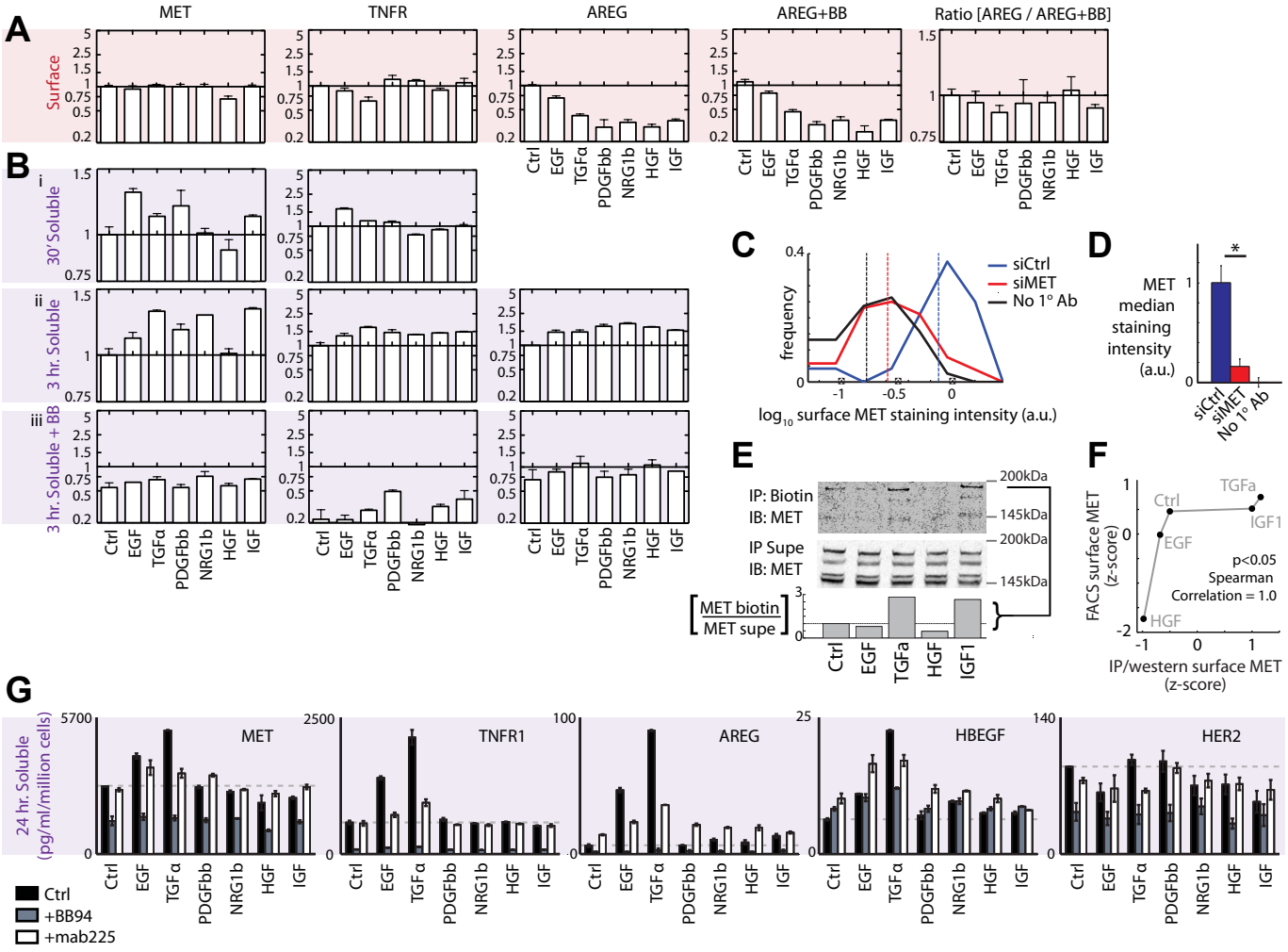

Data shown here were either incorporated directly in the CSR dataset (Figs. 1B-C, 2A), or validate those incorporated measurements. **(A)** Results from live-cell surface immunostaining and cytometry analysis. Data represent the control-normalized averages of measurements taken at 30, 60, and 90 min. post-stimulation, and the left three plots are also shown in Fig. 2A (n=3 biological reps. per growth-factor condition). AREG surface measurements were additionally made following 30 min. pre-treatment with 10uM BB94. Subsequent growth factor stimulation was also in the presence of BB94 ("AREG+BB"). BB94 treatment increased AREG surface levels by an average of 12%. The ratio of surface levels [- BB94] / [+ BB94] (right-most plot) was calculated for each growth factor condition and normalized to the ratio determined under unstimulated conditions. **(B)** *i:* Cellular supernatant was removed from 12Z cell cultures 30 mins. post-stimulation, concentrated using Amicon-ultra 3 kDa size-exclusion columns (Millipore), and analyzed by ELISA (also shown in Fig. 2A; n=3 biological reps.). AREG was not detectable above the sensitivity limit at this time-point. *ii–iii:* Cellular supernatant was removed from 12Z cell cultures 3 hr. post-stimulation and analyzed by ELISA (n=3 reps.; plots from *ii* are included in Fig. 2A). *iii:* Cells were pre-treated 30 min. prior to growth factor stimulation with 10uM BB94, and results were normalized to the untreated control levels detected in the absence of BB94. **(C-D)** siRNA experiments confirm Ab specificity for MET surface levels (see SI-19 for siRNA protocols). Live-cell immunostaining and cytometric analysis show single-cell population distributions of staining intensities (C) and their corresponding averages (D), confirming Ab specificity ($^*p<0.05$). Staining in the absence of a primary Ab treatment but after secondary Ab treatment ("No 1^o Ab") was used to determine background signals. **(E)** Western blotting supports flow-cytometry measurements of surface MET. 30 min. post-stimulation, cells were treated with sulfo-NHS-biotin, lysed, and incubated with streptavidin beads (see SI-19 for protocol). Bound and unbound proteins ("IP:Biotin" and "IP Supe", respectively) were then blotted for MET. The bar-plot shows relative surface MET of the top MW band, quantified by densitometry. **(F)** Mean-centered and variance-normalized (that is, z-score) data from the western blot *E* (x-axis) and flow cytometry *A* (y-axis) indicate perfect rank-order correlation between the two sets of measurements. Poor linearity may be attributed to low signal in the western blot. **(G)** Supernatant analyte concentrations were measured 24 hr. post-stimulation from 12Z grown in the presence of either BB94 or mAb225 (n=2 reps.). All error bars denote S.E.

7 CSR data: single-cell motile response of 12Z to growth factor treatment.

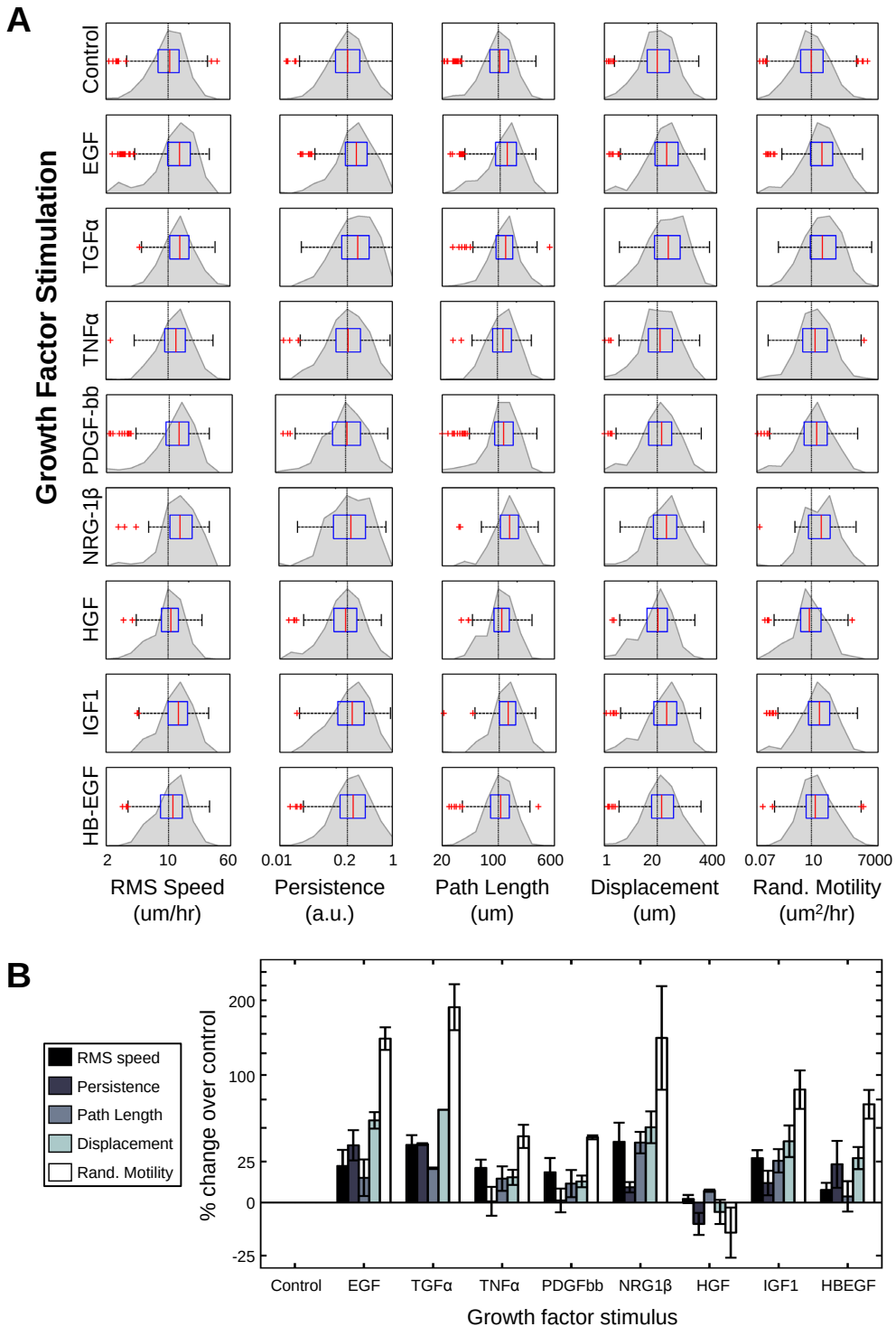

A subset of the data shown here was incorporated directly in the CSR dataset (Figs. 1B-C, 2A). **(A)** Population distributions of single-cell motile response in 12Z. Various descriptive features of cellular motility were computed for individual cells based on single-cell tracking experiments using time-lapse confocal microscopy. Histograms and corresponding box-and-whisker plots show population distributions from single-cell measurements, pooled from n≥2 separate experiments, with ≥100 individual cells for each condition. **(B)** Median population statistics were calculated from the single-cell data shown at top, normalized to the control (+/- S.E. of experimental reps., n≥2 separate populations, with ≥100 cells for each condition). A subset of these data are shown in Figure 2A.

8 Pairwise correlation within the CSR dataset.

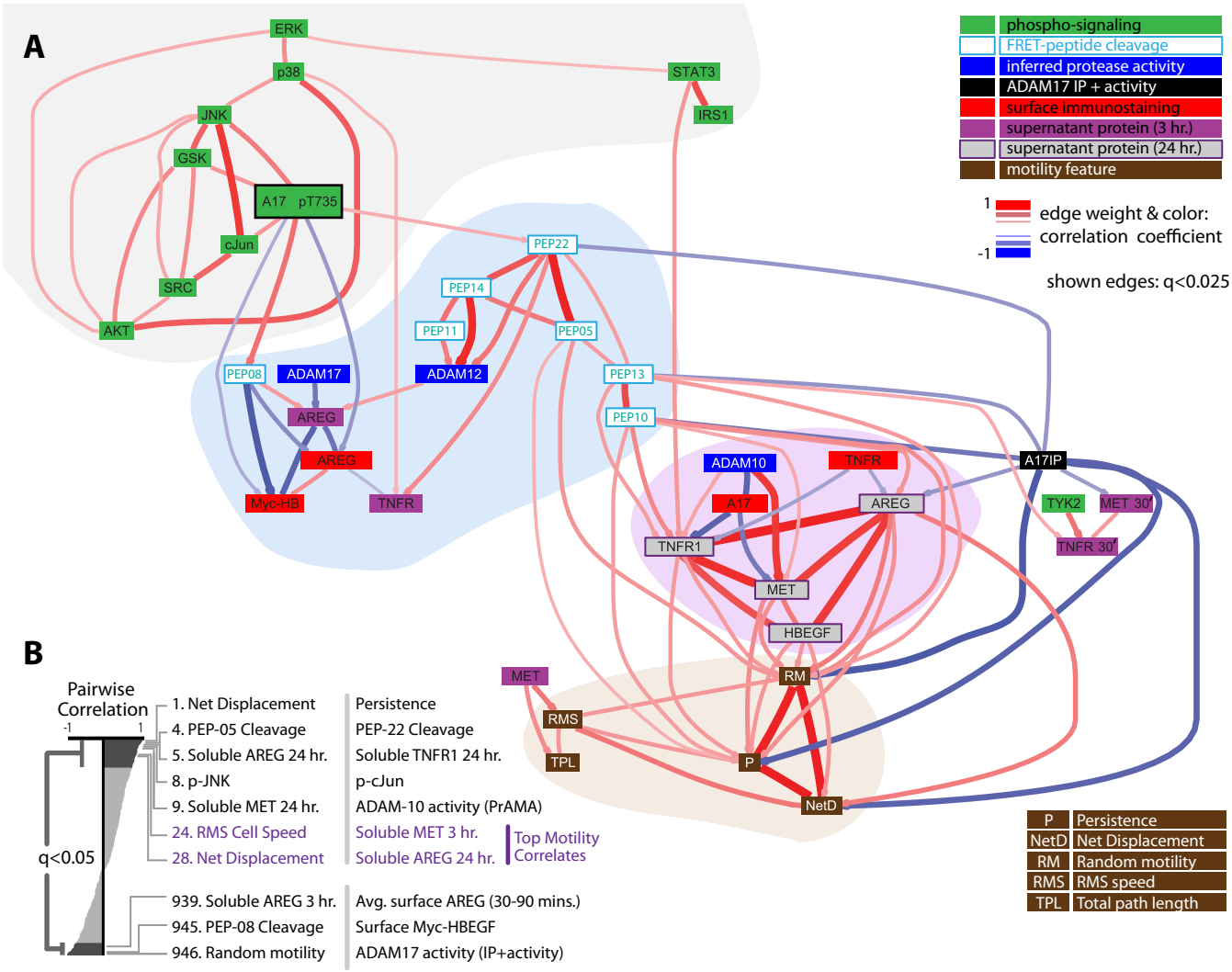

To explore regulatory relationships in the CSR dataset (Fig. 2A), we calculated correlation and corresponding statistical significance among all pairs of variables as they varied across the panel of growth-factor treatments. **(A)** The graphically representated correlation network shows significant correlation (q<0.025; q = multiple hypothesis corrected p-value) among pairs of measurements in the CSR dataset. Node labels and colors correspond by color to Fig. 2. Edge weights and color denote strength and direction of correlation. The correlation graph and spatial organization were generated in an unsupervised, automated manner using the Matlab biograph() function (Mathworks, Natick MA). Shaded areas were manually added to emphasize modularity among the data. Highly interconnected phosho-signaling measurements (top left) link to early protease activity measurements (blue shaded area) primary through ADAM17-pT735. Early protease activity measurements then relate closely to later shedding measurements (purple shaded area), which in turn are highly correlative with features of cell migration (brown). **(B)** All pairwise correlation coefficients depicted in *A* were rank-ordered and shown in the waterfall plot at left. Highly significant correlative pairs are enumerated at right. Somewhat redundant pairs have been omitted from the enumerated list for clarity (for example, the second most correlative pair is very similar to the first: random motility vs. net displacement). For *A*-*B*, both Spearman and Pearson correlation were calculated for each pair of measurements, and the more statistically significant of the two was recorded. P-values based on correlation were calculated using either a Student's t distribution or an approximation of the exact permutation distributions, for Pearson's or Spearman's correlation, respectively. All p-values shown here have been corrected for multiple hypothesis testing using the Storey false discovery rate, and consequently are reported as q-values [55].

9 Multivariate modeling relates sheddase activity to cellular motility.

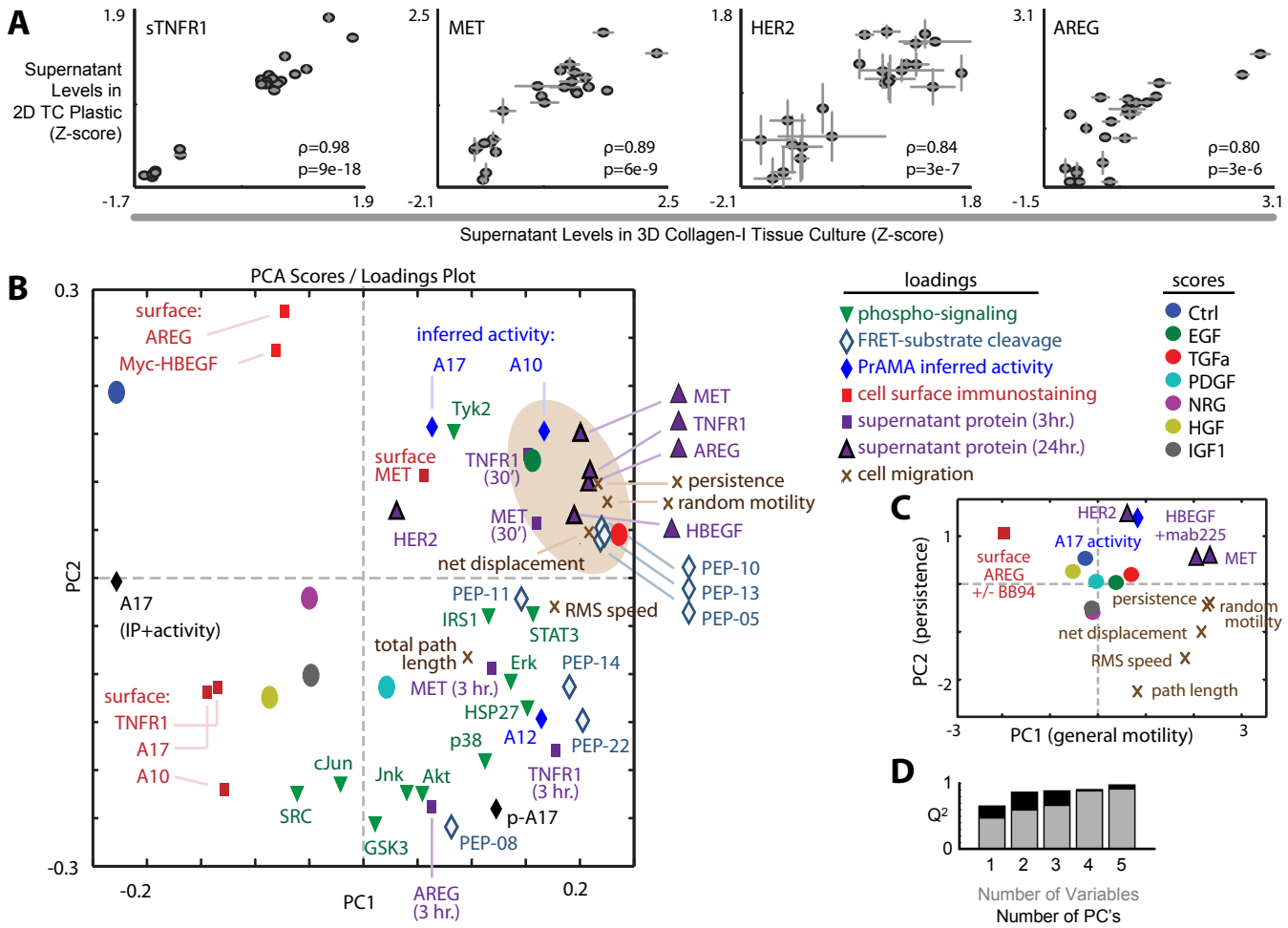

(A) Ligands/receptors included in the CSR dataset (Fig. 2A) exhibit qualitatively similar patterns of accumulation in the supernatant across growth-factor conditions, regardless of 2D or 3D culture environment. Ectodomain shedding was measured in 12Z grown on either tissue culture plastic or in 2.2 mg/ml collagen-I gels. Supernatants from both cell culture environments were collected 24 hr. post-stimulation with the panel of growth factors used in Fig. 2A, in the presence or absence of mab225 and BB94 (n=2 reps., ±S.E.). Spearman's and Pearson's correlation coefficients were calculated for each analyte, and the greater of the two are reported as ρ. P-values based on correlation were calculated using either a Student's t distribution or an approximation of the exact permutation distributions, depending respectively on whether ρ denotes Pearson's or Spearman's correlation. In 3D culture, HBEGF was only detectable above assay sensitivity thresholds under conditions of EGF/TGFa stimulation, and therefore was not included in this analysis. **(B)** This fully labeled depiction of Fig. 2B shows the PCA scores and loadings plot of the entire CSR dataset (Fig. 2A-B). **(C)** This fully labeled depiction of Fig. 2D shows the PLSR scores and loadings plot of the expanded CSR dataset (predictor variables) describing motility features (response variables). The expanded CSR dataset includes measurements made in the presence of BB94 and mab225 across the panel of growth factors (see SI-6). Descriptor variables were iteratively added to the PLSR model to maximize Q^2 prediction accuracy, and two of the five descriptors are not depicted in Fig. 2A: "Surface AREG +/- BB94" denotes the BB94-dependent change in AREG surface levels, and is fully described in SI-6A (right-most graph); "HBEGF+mab225" denotes the levels of supernatant HBEGF detected 24 hr. post-stimulation with growth factors, in the presence of mab225, and is fully described in SI-6G. **(D)** Accurate prediction of motility requires multiple principal components and descriptor variables. PLSR models were constructed as in *C*, but with limits on the number of principal components (black) or descriptor variables (grey, superimposed over black bars) that were allowed to be incorporated into the model structure. Results show that the addition of a second principal component enhances PLSR accuracy by nearly 50%, indicating multiple axes of motility regulation.

10 MMP/TIMP levels poorly correlate with cell migration compared to ligand/receptor shedding.

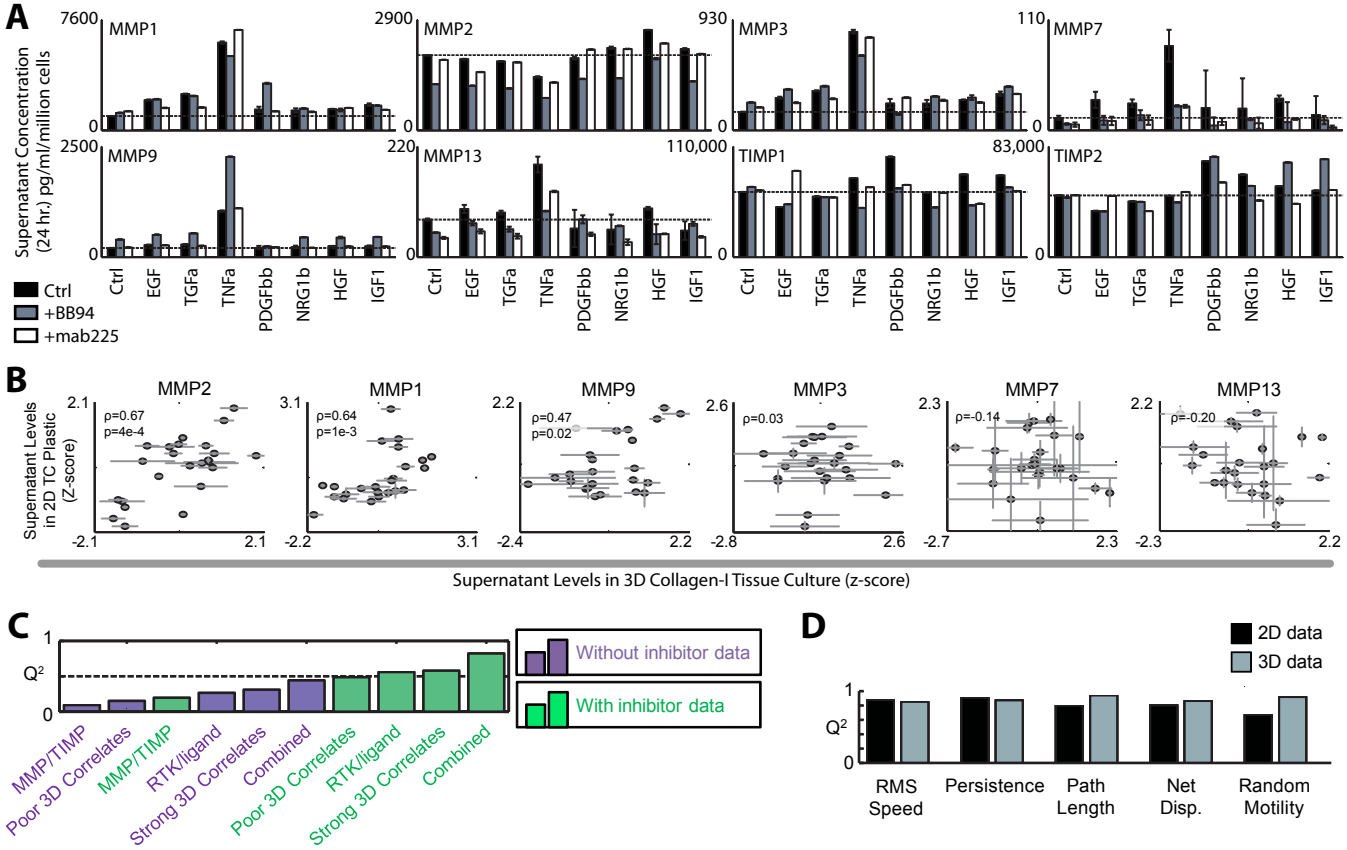

(A) MMP/TIMP supernatant concentrations were measured 24 hr. post-stimulation from 12Z grown on tissue culture plastic in the presence of either BB94 or mAb225 (n=2 reps., ± S.E.). TIMPs have n=1 replicate. **(B)** Compared to ligand/receptor accumulation, MMP/TIMP levels exhibit less consistent patterns of accumulation in the supernatant across growth-factor conditions, depending on 2D or 3D culture environment. Accumulation was measured in 12Z grown on either tissue culture plastic or in 2.2 mg/ml collagen-I gels. Supernatants from both cell culture environments were collected 24 hr. post-stimulation with the panel of growth factors used in Fig. 2A, in the presence or absence of mab225 and BB94 (n=2 reps., ±S.E.). Spearman's and Pearson's correlation coefficients were calculated for each analyte, and the greater of the two are reported as ρ. P-values based on correlation were calculated using either a Student's t distribution or an approximation of the exact permutation distributions, depending respectively on whether ρ denotes Pearson's or Spearman's correlation. **(C)** PLSR models using supernatant measurements emphasize the role for autocrine ligand/RTK shedding over MMP/TIMP secretion in mediating cell migration. PLSR models were constructed to describe cell motility features using various subsets of the supernatant protein concentration data from *A* and SI-6G as descriptor variables. In particular, we decomposed the data into (1) MMP/TIMP vs. RTK/ligand measurements, (2) measurements that significantly vs. insignificantly correlate across 2D and 3D tissue culture environments (using $p<0.05$ as a significance threshold; see *B* and SI-9A), and (3) data including vs. excluding the additional mab225/BB94 treatment for each growth factor condition. Not surprisingly, results show that strong 3D correlate measurements are more accurate predictors of cell migration than poor 3D correlate measurements. Furthermore, results indicate that including measurements of shedding +/- mab225 and BB94 significantly enhances model prediction accuracy, suggesting that these inhibitor treatments reveal additional information regarding metalloproteinase activity and EGFR-autocrine feedback that is relevant to cell migration. Finally, results show that RTK and ligand shedding are more predictive of cell migration than MMP/TIMP secretion patterns, suggeting MMP secretion levels are a relatively poor indicator of their role in cell migration. **(D)** Ectodomain shedding measurements from both 2D and 3D cell cultures equally predict 3D motility. PLSR models were generated to predict cell motility using supernatant measurements collected from cells cultured on either tissue culture plastic (2D) or from cells suspended in collagen I gels (3D) (including ligand/receptor shedding; see *A* and SI-9A). According to Q^2 fitting accuracy, PLSR is capable of using both 2D and 3D supernatant measurements to accurately predict 3D cellular motility. These results are concordant with observed correlation between supernatant measurements in 2D and 3D tissue culture environments (SI-9A).

11 An endpoint collagen-I migration assay captures inhibitor sensitivity.

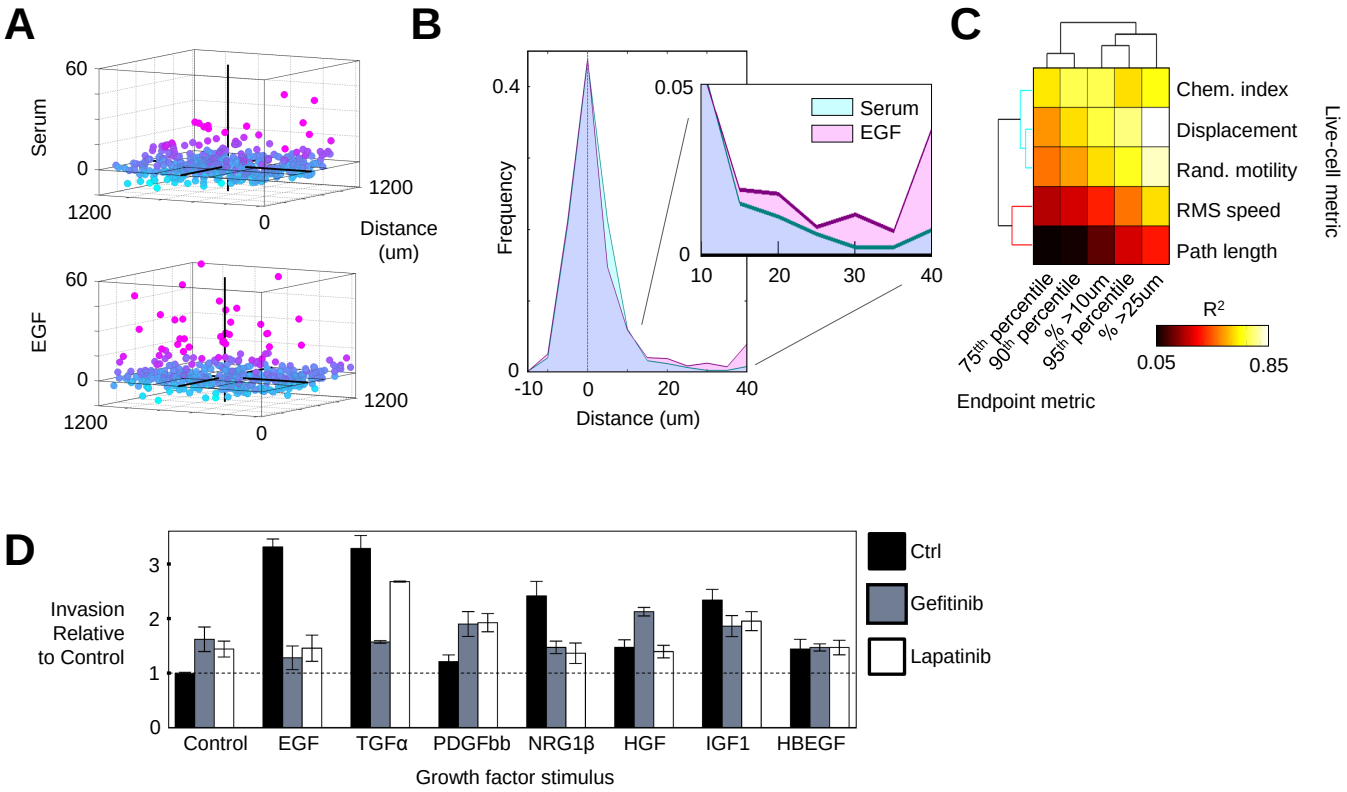

(A) Computationally inferred cell nuclei positions from the endpoint assay, in the presence or absence of EGF, measured 24 hr. post-stimulation (same as Fig. 3E). The x-y plane represents the inferred bottom of the 96-well plate. Nuclei with higher z-coordinates show warmer color. **(B)** Distribution of nuclei z-coordinates, corresponding to *A*. **(C)** Clustergram of correlations between the endpoint assay metrics and median live-cell motility data (live-cell motility data described in SI-7 and Fig. 2A), compared across the panel of growth factors. **(D)** 12Z were stimulated with growth factors following a 1.5 hr. pre-treatment with the EGFR kinase inhibitor, gefitinib, or the dual EGFR/HER-2 kinase inhibitor, lapatinib. Gefitinib results correspond to Fig. 3F-G. The two inhibitors demonstrate similar inhibitory effects, with the exception of TGFa-stimulated motility. One possible explanation for the discrepancy may lie in differences between HER2 shedding under EGF- and TGFa- stimulated conditions (shown in SI-6G): compared to EGF, TGFa stimulates significantly more HER2 shedding ($p<0.05$), and lapatinib (which inhibits HER2) is less effective under TGFa stimulation compared to EGF stimulation. All error bars denote S.E.

12 mAb225 reduces ADAM substrate shedding.

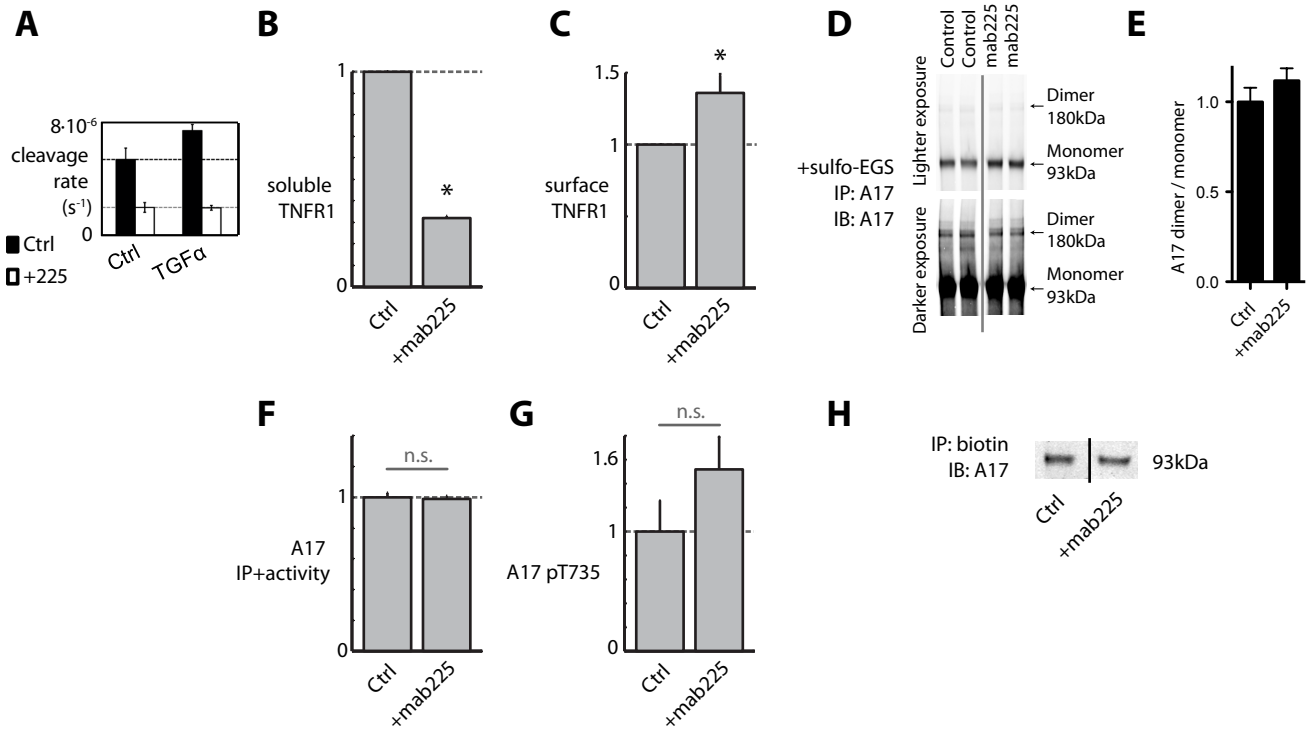

(A) The soluble FRET-substrate PEP-05 was applied concomitantly with TGFa to serum-starved 12Z cultures that had been pre-treated with 10ug/ml mab225 for 30 min., and measured cleavage rates were averaged over the first 3 hr. post-stimulation (n=4 reps.). Cleavage rates of PEP-05, which shares polypeptide sequence similarity to pro-TNFa, were significantly reduced in the presence of mab225. Results correspond to PrAMA inference results shown in Fig. 4A. **(B)** After 30 min. treatment with mab225, cellular supernatant was collected, ultra-concentrated using Amicon-ultra size-exclusion columns (Millipore), and analyzed by ELISA for TNFR1 concentration. Results show significant decrease in TNFR1 shedding with mab225 treatment (n=3 reps.). **(C)** After 1 hr. treatment with mab225, 12Z were surface-immunostained for TNFR1 and anlyzed by flow cytometry. Results indicate a significant increase in surface receptor with mab225 treatment (n=2 experimental reps.). **(D)** Following a 30 min. treatment with mab225, 12Z were treated with sulfo-EGS and lysed. ADAM17 was immunoprecipitated from lysate and then blotted for ADAM17. **(E)** The ratio of dimer-to-monomer band intensities was calculated, and showed no significant difference (n=2 reps.). **(F)** ADAM17 activity was quantified using the Innozyme TACE activity assay (see SI-19 for protocol) from whole-cell lysate collected 45 min. post-treatment with mab225 (n=2 biological reps.) **(G)** ADAM17-pT735 was measured by western blot, quantified by densitometry, and normalized to ACTN1 loading (n=2 reps.). Measurements were taken from whole-cell lysates 30 min. post-stimulation. **(H)** Surface levels of ADAM17 were unchanged by mab225 treatment. Identical numbers of cells were starved in the presence or absence of mab225 for 4 hr., treated with sulfo-NHS-biotin, lysed, and incubated with streptavidin beads (see SI-19 for protocol). Bound proteins were then blotted for ADAM17. All error bars denote S.E., $^*p<0.05$, Student's t-test.

13 Joint RTK and ligand shedding by both ADAM-10 and -17.

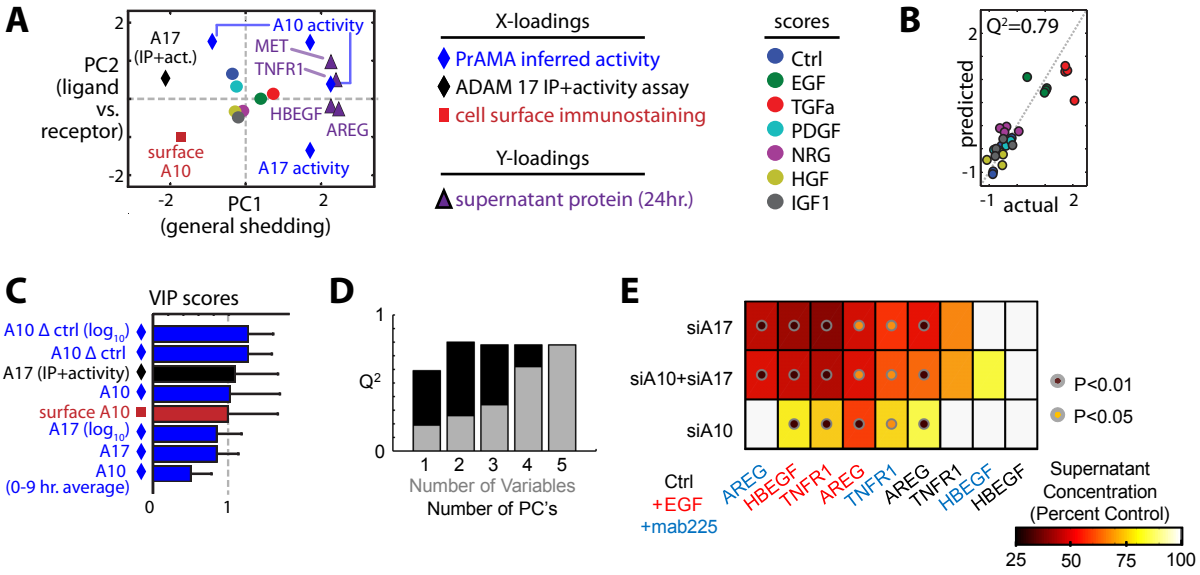

PLSR modeling suggests joint RTK and ligand shedding by both ADAM-10 and -17. PLSR was used to build models that describe AREG, TNFR1, and MET accumulation in the supernatant as a function of phospho-signaling and measured ADAM regulation, across a panel of growth factor treatments (shown in Fig. 2A). To improve model accuracy, we also included FRET-substrate cleavage and PrAMA inference results measured across each of the observed time-points (see SI-3B). The reduced PLSR model only includes descriptor variables that contribute to model prediction accuracy (Q^2), and the final model shown here includes 8 total descriptor variables. **(A)** The scores and loadings plot presents the model in terms of two principal components that chiefly capture general sheddase activity (x-axis) and ligand vs. receptor shedding preference (y-axis). **(B-C)** Q^2 prediction accuracy (B) and the VIP scores (C)for the reduced PLSR model shown in *A*. The PLSR model considered multiple data-transformations of the protease activity data, and included log-transformed data, fold-change normalized data, baseline-subtracted data, as well as activity measurements across multiple time-points. Multiple of these measurements (three for ADAM10, two for ADAM17) were ultimately included in the PLSR model. **(D)** The reduced PLSR model accuracy in *A* improves with the inclusion of multiple descriptor variables (grey bars) and/or PC's (black bars), with two PC's being sufficient to capture 90% of the covariance in the data. This result suggests two axes of regulation govern ligand/receptor shedding, which are described chiefly by ADAM-10 and -17 activities. **(E)** siRNA knockdown of both ADAM-10 and -17 reduces shedding of multiple endogenous substrates. siRNA knockdown results for AREG are also shown in Fig. 4D.

14 Both ADAM-10 and -17 can cleave proAREG.

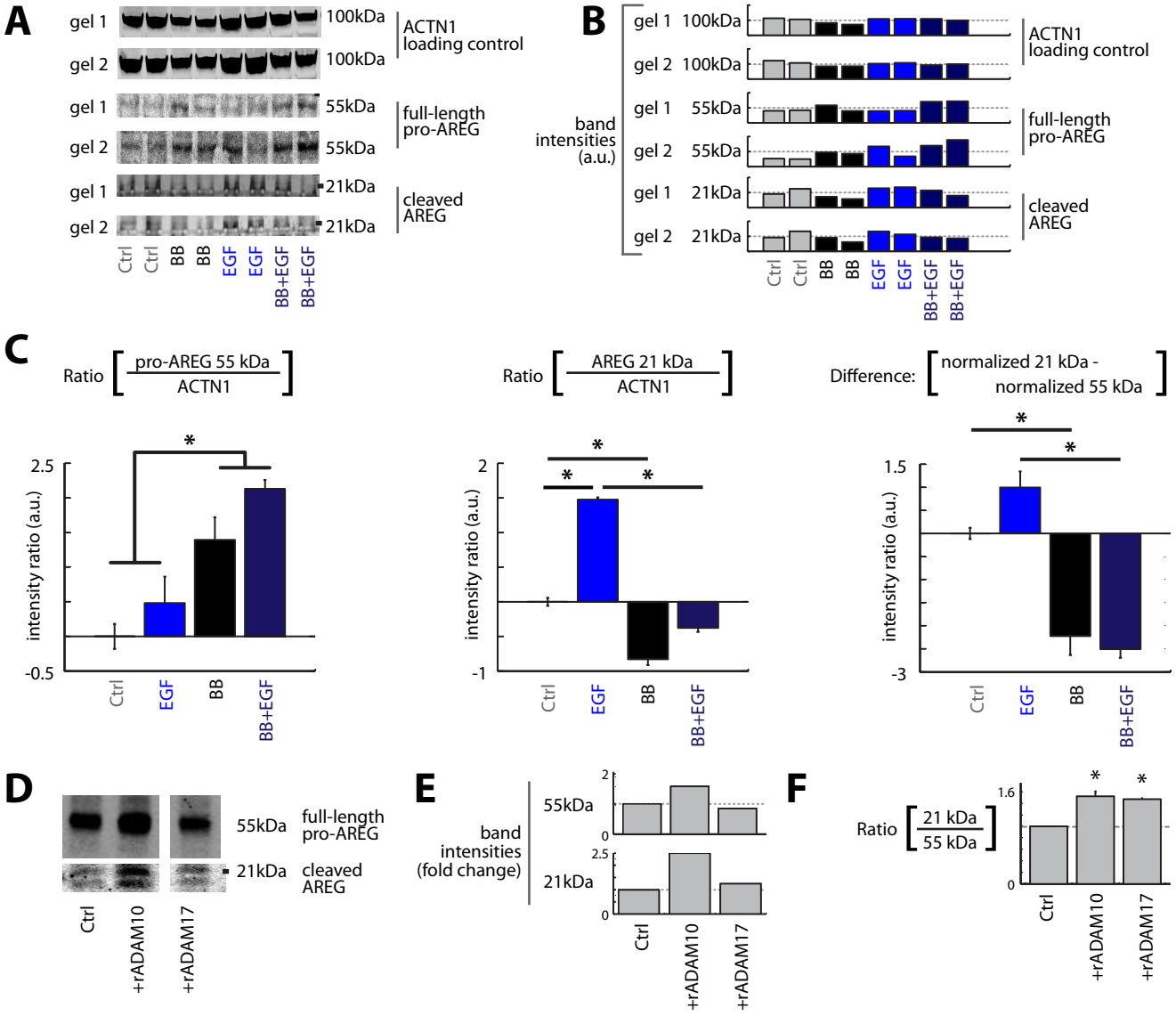

(A-C) Detection of metalloproteinase-dependent AREG degradation in 12Z lysates. 12Z were cultured for 24 hr. following EGF and BB94 treatments, lysed, and blotted for ACTN1 and AREG. Using ectodomain antibodies from the ELISA kit, we focused on two AREG bands that had been previously reported in the literature: full length pro-AREG at roughly 55 kDa, and AREG cleavage products at roughly 21 and 19 kDa [56]. Blot images (A), densitometric quantification (B), and ACTN1-normalized averaging across n=4 replicates (C) demonstrate that EGF treatment causes an increase in the accumulation of the 21 and 19 kDa cleavage products in a metalloproteinase-dependent manner. Furthermore, BB94 treatment leads to an accumulation of the 55 kDa fragment. No 21 kDa cleavage product was visible in blots of the cellular supernatant, which we found unsurprising considering the degree of difficulty detecting AREG even with the more sensitive ELISA format. **(D-F)** pro-AREG digestion with recombinant protease suggests a role for both ADAM-10 and -17. AREG was immunoprecipitated from whole-cell lysate and incubated 4 hr. on-bead with recombinant ADAM-10 and -17. The reaction was boiled in denaturing sample buffer and blotted for AREG, shown by the representative blot in *D*. Full length 55 kDa pro-AREG and the 21/19 kDa band intensities were quantified by densitometry (E), and the ratio of cleavage product to full-length protein significantly increased with both ADAM-10 and -17 digestion (n=2 reps.). All error bars denote S.E., $^{*}p<0.05$, Student's t-test.

15 Proteolytic shedding of HER4 and MET.

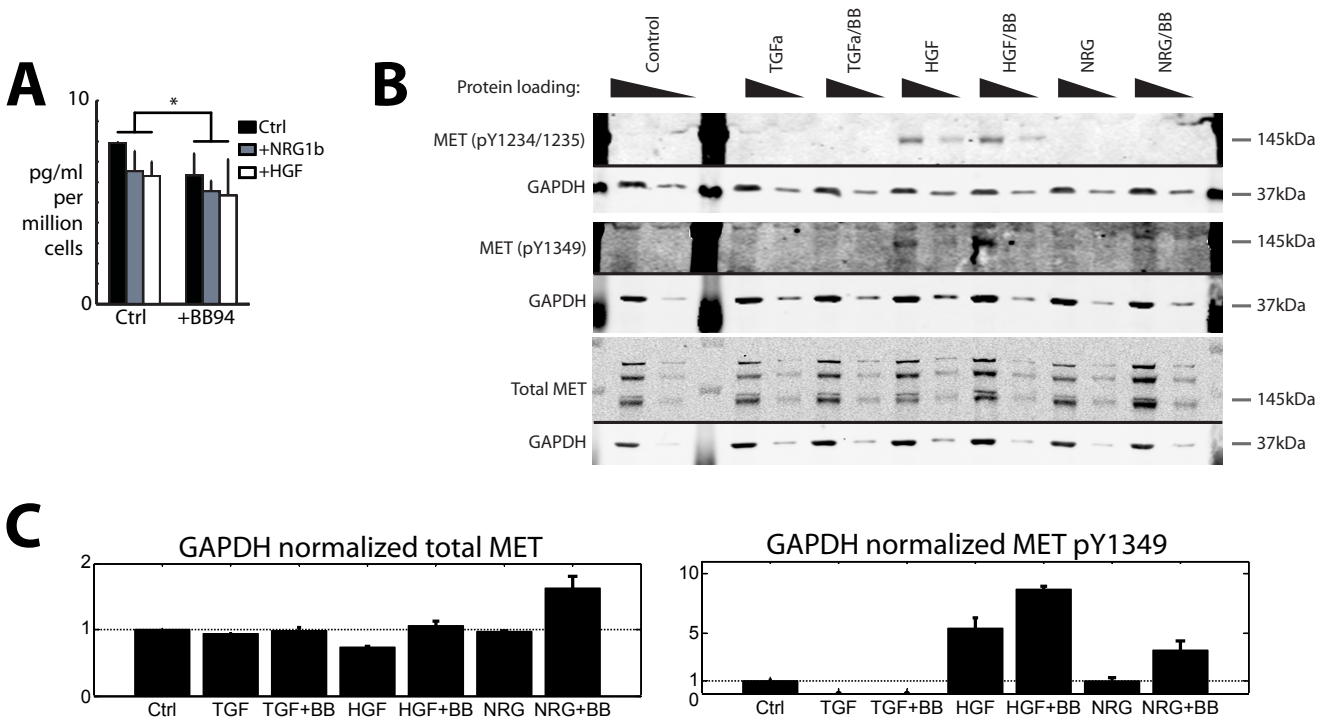

(A) Metalloproteinase inhibition leads to a significant decrease in supernatant HER4 concentration. 12Z were stimulated with growth-factor in the presence or absence of BB94. Supernatant was collected 24 hr. later and analyzed by bead-based ELISA for HER4 concentration (n=2 reps. per condition; $p<0.05$, paired Student's t-test). **(B-C)** Metalloproteinase inhibition leads to an increase in total and pY1349 MET. (B) Representative blot images for quantification of total and phosphorylated MET. After 1.5 hr. pre-treatment with BB94 and 30 min. after stimulation, cells were lysed and blotted for MET, p-MET, and GAPDH. (C) GAPDH-normalized blot quantification (n=2 reps., +/- S.E.), including data from *B*. Total MET was calculated from the sum of all molecular weight bands shown between 145-200 kDa, while pY1349 was quantified from 145 kDa band intensities. BB94 did not significantly change pY1234/34 levels, in contrast to pY1349 levels, which increased with BB94 treatment in the presence of NRG1b and HGF.

16 Effects of kinase inhibition on protease activity and migratory respose to growth factor treatment.

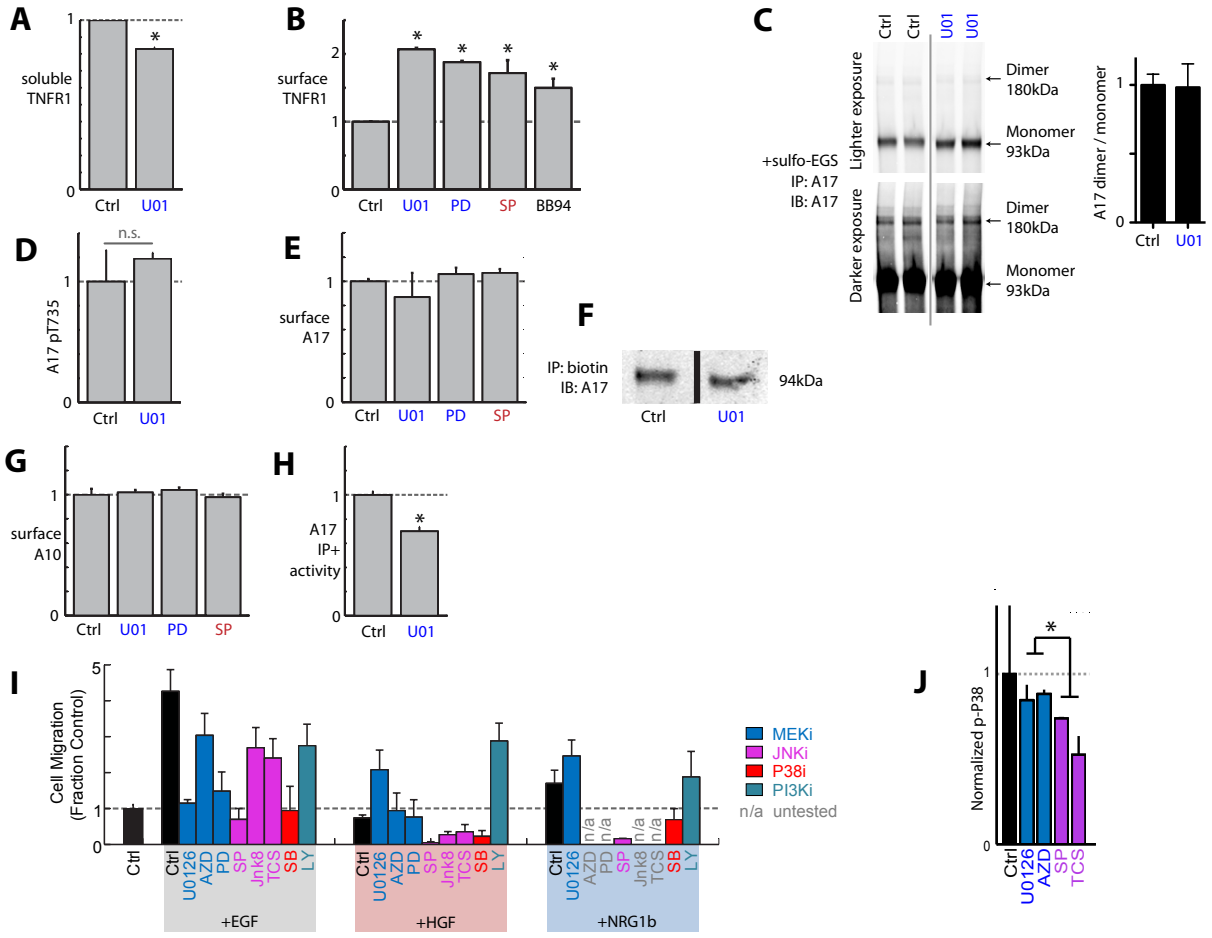

(A) U0126 treatment significantly reduces short-term (30 min.) TNFR1 accumulation in cellular supernatant. After 30 min. treatment with U0126, cellular supernatant was collected, ultra-concentrated using Amicon-ultra size-exclusion columns (Millipore), and analyzed by ELISA for TNFR1 concentration. Results show significant decrease in TNFR1 shedding with U0126 treatment (n=3 reps.). **(B)** Inhibitor treatment increases surface TNFR1 levels. After 1 hr. treatment with signaling and protease inhibitors, 12Z were surface-immunostained for TNFR1 and anlyzed by flow cytometry. Results indicate a significant increase in surface receptor with inhibitor treatment (n=2 experimental reps.). **(C)** ADAM17 dimerization does not significantly change with U0126 treatment. Following a 4 hr. treatment with U0126, 12Z were treated with sulfo-EGS and lysed. ADAM17 was immunoprecipitated from lysate and then blotted for ADAM17. The ratio of dimer-to-monomer band intensities was calculated, and showed no significant difference (n=2 reps.). **(D)** ADAM17-pT735 was measured by western blot, quantified by densitometry, and normalized to ACTN1 loading (n=2 reps.). Measurements were taken from whole-cell lysates 30 min. post-stimulation. **(E)** Surface levels of ADAM17 were unchanged by Mek or Jnk inhibitor treatment. After 1 hr. treatment with signaling inhibitors, 12Z were surface-immunostained for ADAM17 and anlyzed by flow cytometry (n=3 reps.). **(F)** Western blot confirms that U0126 treatment does not influence ADAM17 surface levels. Identical numbers of cells were starved in the presence or absence of U0126 for 4 hr., treated with sulfo-NHS-biotin, lysed, and incubated with streptavidin beads (see SI-19 for protocol). Bound proteins were then blotted for ADAM17. Control-treated band also shown in SI-Appendix Fig. S12H. **(G)** Surface levels of ADAM10 were unchanged by Mek or Jnk inhibitor treatment. After 1 hr. treatment with signaling inhibitors, 12Z were surface-immunostained for ADAM10 and anlyzed by flow cytometry (n=3 reps.). **(H)** ADAM17 activity was quantified using the Innozyme TACE activity assay (see SI-19 for protocol) from whole-cell lysate collected 45 min. post-treatment with U0126 (n=2 biological reps.) **(I)** Mek and PI3K inhibition exhibits context-dependent efficacy and most effectively reduce EGF-stimulated cell migration, whereas Jnk and p38 inhibitors effectively block EGF, HGF, and NRG1b stimulated migration. Using the endpoint cell migration assay (SI-11), cells were pre-treated with inhibitor for 1 hr., followed by growth factor stimulation, and migration was measured 24 hr. later (n≥2 reps.). Data corresponds to the scatter plot shown in Fig. 6E. "n/a" indicates experimental conditions were not tested. **(J)** Jnk inhibitors are more effective than Mek inhibitors at reducing p-p38 levels. Cells were pre-treated with inhibitor for 1.5 hr., stimulated with NRG1b for 5 min., lysed, and analyzed by bead immunoassay. All error bars denote S.E., *p<0.05, Student's t-test.

17 Multivariate analysis of peritoneal fluid proteomics.

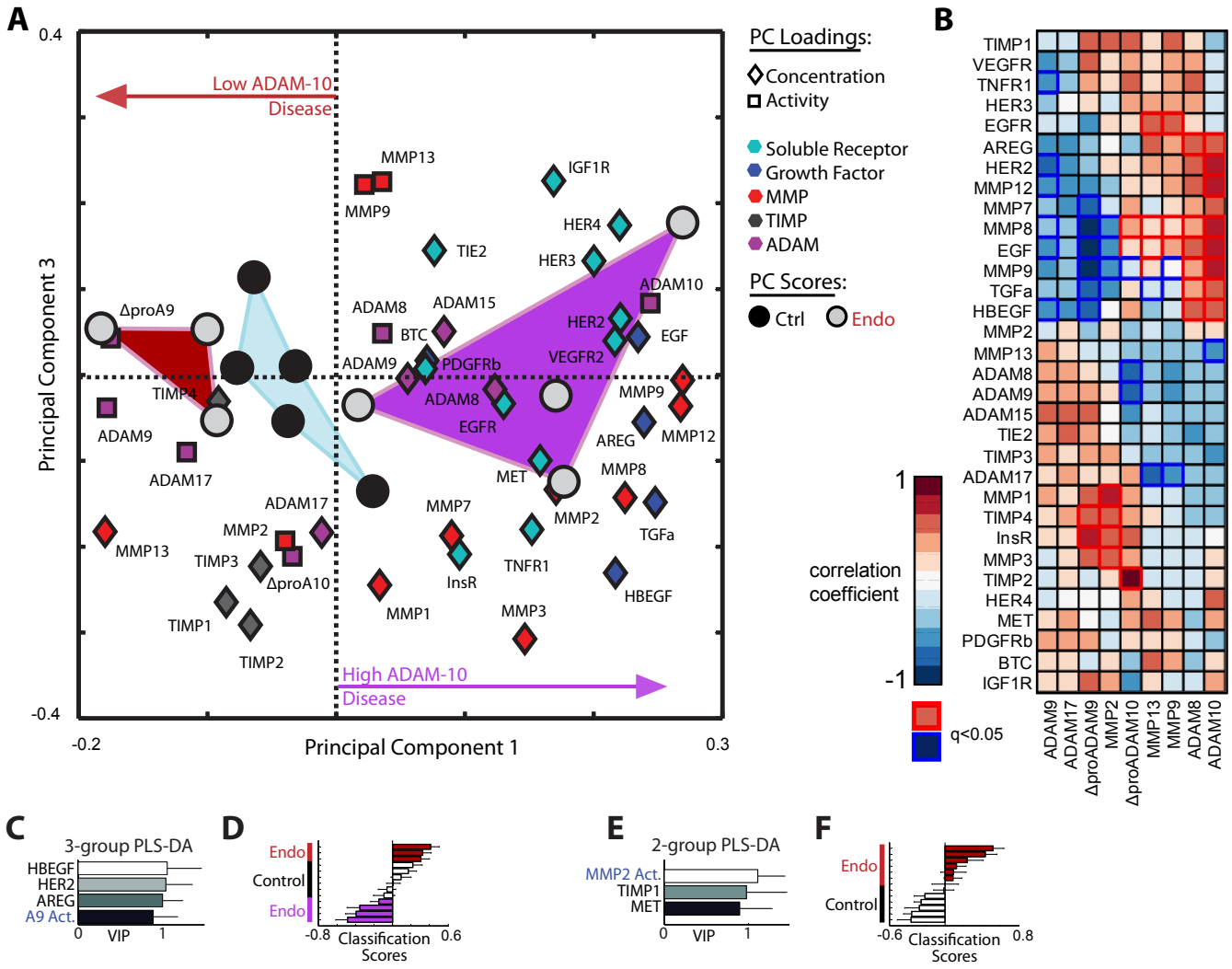

(A) PCA decomposes the protein quantification meaurements (using ELISA) and protease activity measurements (using PrAMA) from the PF samples into key principal components (PCs) of variation. Scores and loadings for PC1 and PC3 are shown here, identical to Fig. 8B, but with complete labeling. ΔproA10 and ΔproA9 denote the difference in observed cleavage rate with and without co-incubation with the specific prodomain inhibitors proADAM9 and proADAM10 (see [53] for greater detail). **(B)** The clustergram, generated by hierarchical biclustering, presents significant correlations between protein levels and protease activities across the PF samples. Spearman's and Pearson's correlation coefficients were calculated between protease activities (columns) and observed analyte concentrations (rows) across the set of thirteen PF samples, and the more statistically significant result is shown. Significance was determined using an approximation of the exact permutation distributions of correlation for the Spearman's correlation, and using a Student's t distribution for the Pearson correlation. P-values were corrected for multiple hypothesis testing using the Storey false discovery rate, and consequently are reported as q-values [55]. **(C-F)** Partial least squares - discriminant analysis (PLS-DA) was used to optimally select a minimal number of descriptor variables that would accurately predict disease state. (C-D) Reduced PLS-DA models were generated to classify samples as falling into one of three states demarcated by the three color groups shown in *A*, using four descriptor measurements (C) and with >95% cross-validation classification accuracy (D). An additional PLS-DA model (E-F) classifies PF samples as either control or disease, using three descriptor measurements (E) and also exhibiting >95% cross-validation classification accuracy (F).

18 AREG, HBEGF, and MET shedding in other disease-relevant cell types.

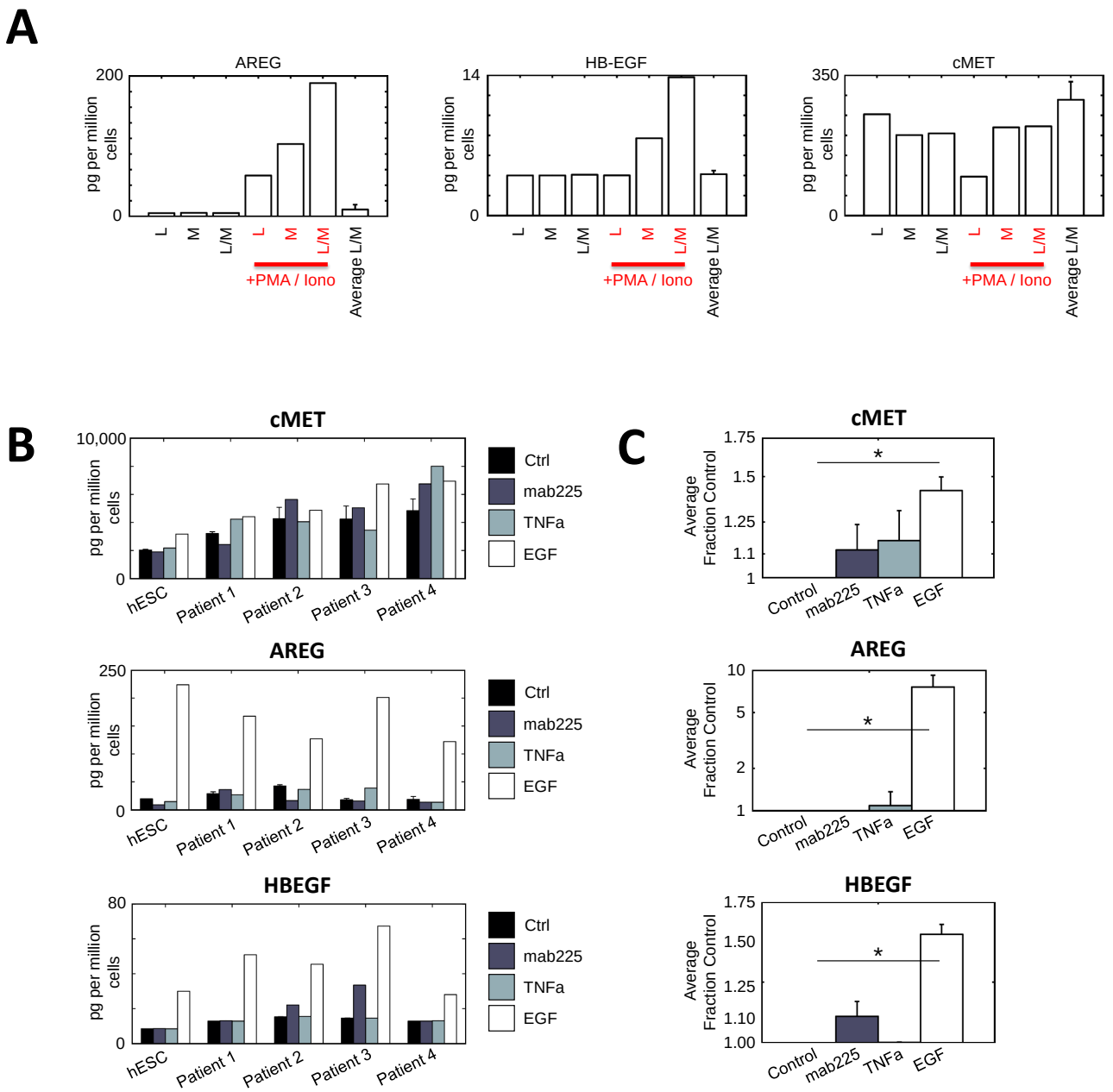

(A) Primary PFMCs shed AREG and HBEGF, but not MET, in response to stimulation. Total PFMCs were separated into adherent, mature monocyte populations (M) and non-adherent lymphocyte populations (L). Cells were stimulated with 10ng/mL PMA and 1ug/mL ionomycin (Iono), supernatant was collected 24 hr. later, and was analyzed by ELISA. "Average L/M" describes the average measurements from PFMC across nine separate patient samples, +/- standard deviation. Results were normalized to cell count and supernatant volume, and correspond to picogram per million cells per day of analyte release. **(B-C)** EGF stimulates significant AREG, MET, and HBEGF in endometrial stromal cells. Telomerase-immortalized endometrial stromal cells (tHESC) and primary endometrial stromal cultures from four patients were assayed for ligand and receptor shedding 24 hr. after treatment with either EGF, TNFa, or mab225. Results were normalized to cell count and supernatant volume, and correspond to picogram per million cells per day of analyte release. (C) Shedding induction was calculated relative to basal levels and averaged across all five samples ($^*p<0.05$, paired Student's t-test).

19 Materials and Methods.

Growth factors and inhibitors: Recombinant growth factors and cytokines were purchased from Peprotech (Rocky Hill, NJ). For all experiments, EGF was used at a final concentration of 100ng/mL, NRG1β was used at 80ng/mL, and all others were used at 50ng/mL. Inhibitors used in this paper, their final concentrations, and vendor source are as follows: BB94 (metalloproteinase inh.; 10uM; Tocris Bioscience), mAb225 (EGFR blocking mAb; 10ug/ml; purified from the ATCC hybridoma), gefitinib (EGFR inh.; 1uM; LC Labs), lapatinib (EGFR/HER2 inh.; 1uM; LC Labs), SP600125 (Jnk inh.; 20uM; LC Labs), TCS-6o (Jnk inh.; 10uM; Tocris), Jnk-IN-8 (Jnk inh.; 3uM; generously provided by the Gray Lab, Harvard Medical School), SB203580 (P38 inh.; 20uM; LC Labs), LY294002 (PI3K inh.; 10uM; LC Labs), U0126 (Mek inh.; 10uM; LC Labs), AZD6244 (Mek inh.; 5uM; Selleck Chem.), PD0325901 (Mek inh.; 10uM; Tocris), Foretinib (MET inh.; 100nM; Selleck), α-AREG mAb (AREG inh.; 10ug/ml; R&D Systems), pro-ADAM-9 (ADAM-9 inh.; 10uM; Biozyme, Inc.; Apex, NC), pro-ADAM-10 (ADAM-10 inh.; 4uM; Biozyme, Inc.).

Tissue culture: The 12Z cell line was generously provided by Anna Starzinski-Powitz (University of Frankfurt) by way of Steve Palmer (EMD Serono). Telomerase-immortalized human endometrial fibroblasts (tHESC CRL-4003; ATCC) were cultured according to supplier recommendations. 12Z were routinely cultured in media that consisted of DMEM/F12 supplemented with 100 U/ml penicillin, 100μg/ml streptomycin (Invitrogen), along with 10% fetal bovine serum (Atlanta Biologicals; Atlanta, GA) at 37^{o}C, 5% CO_2. Excluding cell migration assays, 12Z were serum starved for at least 4 hr. before all experiments.

Immunoassays: Phospho-protein levels were measured using the following bead-based sandwich immunoassays (Bio-Rad; Hercules, CA): p-Akt(Ser473), p-cJun(Ser63), p-ERK1/2(Thr202/Tyr204, Thr185/Tyr187), p-HSP27(Ser78), p-Jnk(Thr183/Tyr185), p-p38(Thr180/Tyr182), p-Src(Tyr416), p-STAT3(Tyr705), p-GSK3a/b(Ser21/Ser9), p-Tyk2(Tyr1054/Tyr1055),
and p-IRS-1(Ser636/Ser639). Site-specific p-EGFR(Tyr1173) Ab was used in Fig. 3B. Other EGFR, HER2, and HER4 phosphorylation levels were measured using a bead-conjugated ectodomain capture Ab and a pan-phosphotyrosine detection Ab (EMD4Biosciences). Supernatant ligand, receptor, MMP, and TIMP measurements were performed using R&D Duo-set ELISA kits (R&D Systems, Minneapolis, MN), Widescreen bead-based ELISAs from EMD4Biosciences (Merck KGaA, Darmstadt, Germany), and Fluorokine MAP Multiplex kits (R&D Systems). p-MET western blots used clone D26 for p-MET(Tyr1234/1235) and clone 130H2 for p-MET(Tyr1349), both from Cell Signaling Technologies (Danvers, MA). ADAM17 western blots used a rabbit polyclonal Ab (Ab2051; Abcam). ADAM10 western blots used a rabbit polyclonal Ab targeting amino acids 732-748 (Sigma). Western blots were imaged using an Odyssey (Li-cor) infrared scanner and dye-conjugated secondary antibodies (Invitrogen). AREG western blots used ectodomain AREG antibodies from the R&D Systems Duo-set. All blot images were processed using standard ImageJ functions for contrast adjustment, background subtraction, and densitometry, in accordance with publication guidelines.

Immunostaining and flow cytometry: Immunostaining and flow cytometry were used to assess surface levels of ADAM10, ADAM17, and sheddase substrates. For these measurements, cells were treated with trypsin/EDTA (Gibco) for 15 min., rinsed in 4^{o}C PBS + 3% FBS, and incubated with primary antibodies at 1:100 dilution for 2 hr. in 4^{o}C PBS + 3% FBS. Cells were rinsed in 4^{o}C PBS + 3% FBS, fixed in 2% PFA + PBS overnight, and stained with secondary antibody the following day. Flow cytometry was performed using the BD Biosciences LSR-II. ADAM10 ectodomain mAb (clone 163003) and antibodies from R&D Duo-set kits were used for immunostaining.

ADAM17 Dimerization: Confluent 15 cm plates of 12Z cells were starved for 4 hr. and then stimulated for 30 min. with the indicated growth factor. After washing with 4^{o}C PBS, cells were incubated with 0.5 mg/mL sulfo-EGS (Pierce) for 30 min., then lysed in 1% NP40 lysis buffer. Lysates were clarified, precleared with agarose resin, and then incubated with protein A/G resin (Pierce) and anti-ADAM17 antibody (R&D Systems Duo-set) overnight. The next day, the resin was washed repeatedly, and then boiled in denaturing lysis buffer to elute protein. Dimerized ADAM17 was identified by western according to size shift, and normalized to the monomer ADAM17 in each sample. Methods roughly follow previously work describing ADAM-17 dimerization [57].

IP/western surface protein measurements: Identical numbers of cells were starved in the presence or absence of inhibitor for 4 hr., and then surface biotinylated with 0.5 mg/mL S-NHS-biotin (Pierce) for 30 min. at 4^{o}C. Lysate was clarified, precleared with unconjugated sepharose resin for 1 hr. (Invitrogen), and incubated with straptavidin-conjugated sepharose resin (Invitrogen) overnight. After washing, the bound fraction was eluted by boiling in denaturing sample buffer.

AREG immunoprecipitation and digestion: Four 15 cm plates of 12Z were lysed in 1% NP40 lysis buffer, clarified, and then incubated with protein A/G resin (Pierce) and 10 ug anti-AREG antibody (R&D Systems Duo-set) overnight. After repeated washing, the resin was split into separate samples for digest. Roughly 5nM active recombinant ADAM-10 and -17 (R&D Systems) were incubated with resin for 4 hr. The reaction was then boiled in denaturing sample buffer, and cleavage products were blotted using ectodomain AREG antibodies from the R&D Systems Duo-set kit. The 55kDa band was detected with the polyclonal goat IgG Ab, while the immunopurification and 19/21 kDa bands were performed using the mouse IgG mAb.

Peritoneal fluid sample and analysis: Peritoneal fluid, primary HESC, and PFMC samples were all from patients who provided informed consent in accordance with a protocol approved by the Partners Human Research Committee and the Massachusetts Institute of Technology Committee on the Use of Humans as Experimental Subjects. We limited enrollment to pre-menopausal women with regular cycles (26-32 days), and excluded subjects having received hormone treatment within three months of surgery. Moderate/Severe

(Stage III/IV) endometriosis was laparscopically diagnosed based on the revised criteria of the American Society for Reproductive Medicine [58]. Control samples were free of visible endometriosis and typically received laparoscopy for reasons relating to abdominal pain and/or symptomatic uterine fibroids. Peritoneal fluid was aspirated during laparoscopy from the rectouterine pouch, following trocar insertion and before lavage or surgical manipulation. Specimens were immediately clarified within 15 min. by centrifugation, aliquoted, and stored at -80^{o}C until further analysis.

Primary and immortalized HESC: Endometrial tissue was obtained from pipelle uterine biopsies of normally cycling pre-menopausal women. Isolation and purification of endometrial stromal fibroblasts was performed as previously described [59]. Briefly, tissue was dissected into approximately 1mm^3 fragments using a sterile scalpel blade, transferred into a tube containing fresh complete media and centrifuged (400xg) to eliminate excess blood and debris. Fragments were resuspended in an enzyme mix containing 0.5% collagenase type IV and 0.02% deoxyribonuclease I, and 2% chicken serum in phenol red-free DMEM-F12. Suspensions were incubated at 37^{o}C for 1 hr., intermittently aspirated through decreasing sizes of glass pipettes for cell dispersion, and finally filtered through a 100um and subsequently 70um nylon cell strainer.

PFMC isolation and media conditioning: Peritoneal fluid mononuclear cells were isolated from fresh peritoneal aspirates by centrifugation (10 min. at 1000xg) and cryopreserved in complete media supplemented with 10% DMSO. Upon thawing, cells were washed and seeded at 100,000 cells/cm^2 in 24-well plates for selective adherence of mature monocytes. Non-adherent populations were removed by gentle washing after three hours of culture, and conditioned media collected following an additional 24 hours of monocyte-enriched culture. Flow cytometry routinely indicated >99% CD45 expression in fresh PFMC suspensions and >90% lymphocyte depletion in monocyte-enriched preparations.

ADAM17 IP & activity assay: ADAM17 was precipitated on an anti-ADAM17 coated 96-well plate and incubated with a FRET-based protease substrate. Increase in fluorescence was tracked over time for 4 hr. The slope of increase was calculated and compared to a standard dilution series according to the manufacturer's instructions (Innozyme TACE activity assay, EMD Millipore, Billerica MA). In all cases, cleavage rates were detected within the dynamic range of the assay according to the standard curve.

Supernatant analysis: For quantification of supernatant analytes (Figs. 2A, 3A, 4C-D, 6A, SI-6G, SI-10A, SI-15A), cells were plated on polystyrene plates (Corning) at 80% confluency, and stimulated the following day with serum-free media supplemented with growth factors after a 30min. pre-treatment with inhibitor. 12Z were serum starved overnight before treatment. Supernatant was collected 24 hr. after stimulation, clarified by centrifugation (5min., 300g), and frozen at -20^{o}C for storage. At the time of supernatant collection, cells were trypsinized and analyzed for cell count and viability using ViCell instrumentation (Beckman Coulter; Brea, CA). Final analyte concentration measurements were normalized to cell count.

siRNA knockdown protocol: siRNA treatments used ON-TARGETplus SMARTpool siRNAs (Thermo Scientific), with siGENOME non-targeting siRNA pool-2 as the negative control. 0.5 million cells were seeded in 10 cm dishes. The following day the cells were transfected using 5 uL Dharmafect 4 and 125 pmol siRNA according to the manufacturer's protocol. One day after transfection, cells were reseeded for knockdown experiments, and 48 hr. after transfection cells were treated and lysed. Experiments for measuring ectodomain shedding and cell migration began with growth-factor stimulation 48 hr. post-transfection, and ended 24 hr. later (48 hr. later, for Fig. 7D).

Migration assay computation: To interpret live-cell migration experiments, the root-mean-squared cell speed was calculated from position intervals between time points for each cell track, as well as the standard deviation of the mean [60, 61]. In this work, persistence denotes net displacement divided by the total path length. Endpoint migration assays were interpreted using a modified spot finding algorithm [62] in Matlab (Mathworks; Natick, MA). Briefly, confocal z-stacks were first pre-processed using background subtraction to eliminate uneven microscope illumination, followed by top-hat filtering and contrast enhancement. Pre-processed images were segmented using previously described software [62]. Identified nuclei positions were assessed by nearest-neighbor analysis and PCA to infer the well-bottom where the majority of cells reside, and z-positions of the nuclei were determined as a distance from the xy-plane of the well-bottom. Unless otherwise stated, migration metrics were calculated as a fraction of cells that had invaded further than 20um from the well-bottom, although this threshold slightly changed depending on day-to-day variability to maximize signal-to-noise and minimize background.

Partial least squares analysis: Partial least squares regression (PLSR), partial least squares discriminant analysis (PLS-DA), principal component analysis (PCA), hierarchical biclustering, and all other statistical analyses were performed using Matlab (Mathworks; Natick, MA). Unless otherwise stated, all input and output variables were mean-centered and variance-normalized across the set of environmental stimuli, prior to PLSR, PLS-DA, or PCA. For PLSR and PLS-DA, we implemented a forward-variable selection procedure to heuristically select the minimal combination of input variables that optimally described output variable response. We iteratively added input variables to the PLSR model if they improved model fit as determined by leave-one-out cross validation accuracy. To avoid local optima, we conducted heuristic searches with several cost functions of the cross-validation accuracy, including Q^2 (the R^2 coefficient of determination for prediction accuracy), Spearman rank correlation, Pearson correlation coefficients, and for PLS-DA, area under the R.O.C. curve (AUROC). To avoid over-fitting, we required the added input variables to demonstrate PLSR loadings of greater magnitude than their observed loading standard error. Variable importance in the projection (VIP) statistics were calculated in the usual manner. Standard error for scores, loadings, and VIP were calculated by the jack-knife [63]. Variance of the prediction values

were computed according to Höskuldsson [64]. All results presented in this work with non-zero Q^2 or AUROC accuracy demonstrated a statistical significance ($p<0.05$) as determined by the permutation test. Briefly, we randomly shuffled output variables relative to the model inputs, and ran the variable-selection procedure for each of 1000 random permutations. Shuffled data yielded a lower Q^2 value than that achieved by the actual data-set more than 95% of the time.

References

[1] Kyama CM, Overbergh L, Debrock S, Valckx D, Vander Perre S, et al. (2006) Increased peritoneal and endometrial gene expression of biologically relevant cytokines and growth factors during the menstrual phase in women with endometriosis. Fertil Steril 85: 1667–1675.

[2] Bedaiwy MA, Falcone T, Sharma RK, Goldberg JM, Attaran M, et al. (2002) Prediction of endometriosis with serum and peritoneal fluid markers: a prospective controlled trial. Hum Reprod 17: 426–431.

[3] Overton C, Fernandez-Shaw S, Hicks B, Barlow D, Starkey P (1996) Peritoneal fluid cytokines and the relationship with endometriosis and pain. Hum Reprod 11: 380–386.

[4] Xavier P, Belo L, Beires J, Rebelo I, Martinez-de Oliveira J, et al. (2006) Serum levels of VEGF and TNF-α and their association with C-reactive protein in patients with endometriosis. Arch Gynecol Obstet 273: 227–231.

[5] Pizzo A, Salmeri FM, Ardita FV, Sofo V, Tripepi M, et al. (2002) Behaviour of cytokine levels in serum and peritoneal fluid of women with endometriosis. Gynecol Obstet Invest 54: 82–87.

[6] De Leon FD, Vijayakumar R, Brown M, Rao CV, Yussman MA, et al. (1986) Peritoneal fluid volume, estrogen, progesterone, prostaglandin, and epidermal growth factor concentrations in patients with and without endometriosis. Obstet Gynecol 68: 189–194.

[7] Huang JC, Papasakelariou C, Dawood MY (1996) Epidermal growth factor and basic fibroblast growth factor in peritoneal fluid of women with endometriosis. Fertil Steril 65: 931–934.

[8] Simms JS, Chegini N, Williams RS, Rossi AM, Dunn WA Jr (1991) Identification of epidermal growth factor, transforming growth factor-alpha, and epidermal growth factor receptor in surgically induced endometriosis in rats. Obstet Gynecol 78: 850–857.

[9] Sheng Q, Liu X, Fleming E, Yuan K, Piao H, et al. (2010) An activated ERBB3/NRG1 autocrine loop supports in vivo proliferation in ovarian cancer cells. Cancer Cell 17: 298–310.

[10] Kalu E, Sumar N, Giannopoulos T, Patel P, Croucher C, et al. (2007) Cytokine profiles in serum and peritoneal fluid from infertile women with and without endometriosis. J Obstet Gynaecol Res 33: 490–495.

[11] Osuga Y, Tsutsumi O, Okagaki R, Takai Y, Fujimoto A, et al. (1999) Hepatocyte growth factor concentrations are elevated in peritoneal fluid of women with endometriosis. Hum Reprod 14: 1611–1613.

[12] Matalliotakis IM, Goumenou AG, Koumantakis GE, Neonaki MA, Koumantakis EE, et al. (2003) Serum concentrations of growth factors in women with and without endometriosis: the action of anti-endometriosis medicines. Int Immunopharmacol 3: 81–89.

[13] Steff AM, Gagné D, Page M, Rioux A, Hugo P, et al. (2004) Serum concentrations of insulin-like growth factor-1, soluble tumor necrosis factor receptor-1 and angiogenin in endometriosis patients. Am J Reprod Immunol 51: 166–173.

[14] Gurgan T, Bukulmez O, Yarali H, Tanir M, Akyildiz S (1999) Serum and peritoneal fluid levels of IGF I and II and insulinlike growth binding protein-3 in endometriosis. J Reprod Med 44: 450–454.

[15] Yoshino O, Osuga Y, Hirota Y, Koga K, Hirata T, et al. (2004) Possible pathophysiological roles of Mitogen-Activated Protein Kinases (MAPKs) in endometriosis. Am J Reprod Immunol 52: 306–311.

[16] Yoshino O, Osuga Y, Koga K, Hirota Y, Hirata T, et al. (2006) FR 167653, a p38 mitogen-activated protein kinase inhibitor, suppresses the development of endometriosis in a murine model. J Reprod Immunol 72: 85–93.

[17] Zhou WD, Yang HM, Wang Q, Su DY, Liu FA, et al. (2010) SB203580, a p38 mitogen-activated protein kinase inhibitor, suppresses the development of endometriosis by down-regulating proinflammatory cytokines and proteolytic factors in a mouse model. Hum Reprod 25: 3110–3116.

[18] Murk W, Atabekoglu CS, Cakmak H, Heper A, Ensari A, et al. (2008) Extracellularly signal-regulated kinase activity in the human endometrium: possible roles in the pathogenesis of endometriosis. J Clin Endocrinol Metab 93: 3532–3540.

[19] Honda H, Barrueto FF, Gogusev J, Im DD, Morin PJ (2008) Serial analysis of gene expression reveals differential expression between endometriosis and normal endometrium. Possible roles for AXL and SHC1 in the pathogenesis of endometriosis. Reprod Biol Endocrinol 6: 59.

[20] Uz YH, Murk W, Bozkurt I, Kizilay G, Arici A, et al. (2011) Increased c-Jun N-terminal kinase activation in human endometriotic endothelial cells. Histochem Cell Biol 135: 83–91.

[21] Yousef MHM, Chai DC, Mwenda JM, D'Hooghe TM (2009) The effect of JNK-inhibitors on endometriosis in baboons with induced disease: a placebo-controlled randomized study. Fertil Steril 92: S11.

[22] Matsuzaki S, Canis M, Vaurs-Barrire C, Pouly JL, Boespflug-Tanguy O, et al. (2004) DNA microarray analysis of gene expression profiles in deep endometriosis using laser capture microdissection. Mol Hum Reprod 10: 719–728.

[23] El-Ghobashy AA, Shaaban AM, Innes J, Prime W, Herrington CS (2005) Upregulation of heat shock protein 27 in metaplastic and neoplastic lesions of the endocervix. Int J Gynecol Cancer 15: 503–509.

[24] Shazand K, Baban S, Priv C, Malette B, Croteau P, et al. (2004) FOXO1 and c-jun transcription factors mRNA are modulated in endometriosis. Mol Hum Reprod 10: 871–877.

[25] Ohlsson Teague EM, Van der Hoek KH, Van der Hoek MB, Perry N, Wagaarachchi P, et al. (2009) MicroRNA-regulated pathways associated with endometriosis. Mol Endocrinol 23: 265–275.

[26] Cinar O, Seval Y, Uz YH, Cakmak H, Ulukus M, et al. (2009) Differential regulation of Akt phosphorylation in endometriosis. Reprod Biomed Online 19: 864–871.

[27] Laudanski P, Szamatowicz J, Kowalczuk O, Kuzmicki M, Grabowicz M, et al. (2009) Expression of selected tumor suppressor and oncogenes in endometrium of women with endometriosis. Hum Reprod 24: 1880–1890.

[28] Itoh F, Komohara Y, Takaishi K, Honda R, Tashiro H, et al. (2013) Possible involvement of signal transducer and activator of transcription-3 in cell-cell interactions of peritoneal macrophages and endometrial stromal cells in human endometriosis. Mol Cell Endocrinol doi: 10.1016/j.fertnstert.2013.01.133. [Epub ahead of print].

[29] Lee J, Banu SK, Burghardt RC, Starzinski-Powitz A, Arosh JA (2012) Selective inhibition of prostaglandin E2 receptors EP2 and EP4 inhibits adhesion of human endometriotic epithelial and stromal cells through suppression of integrin-mediated mechanisms. Biol Reprod Dec 12 [Epub ahead of print].

[30] Lee J, Banu SK, Subbarao T, Starzinski-Powitz A, Arosh JA (2012) Selective inhibition of prostaglandin E2 receptors EP2 and EP4 inhibits invasion of human immortalized endometriotic epithelial and stromal cells through suppression of metalloproteinases. Mol Cell Endocrinol 332: 306–313.

[31] Cayan F, Ertun D, Aras-Ates N, Ayaz L, Akbay E, et al. (2010) Association of G1057D variant of insulin receptor substrate-2 with endometriosis. Fertil Steril 94: 1622–1626.

[32] Peluso C, Christofolini DM, Goldman CS, Mafra FA, Cavalcanti V, et al. (2012) TYK2 rs34536443 polymorphism is associated with a decreased susceptibility to endometriosis-related infertility. Hum Immunol 74: 93–97.

[33] Ejskjaer K, Sorensen BS, Poulsen SS, Mogensen O, Forman A, Nexo E (2009) Expression of the epidermal growth factor system in eutopic endometrium from women with endometriosis differs from that in endometrium from healthy women. Gynecol Obstet Invest 67:118-126.

[34] Uzan C, Darai E, Valent A, Graesslin O, Cortez A, et al. (2009) Status of HER1 and HER2 in peritoneal, ovarian and colorectal endometriosis and ovarian endometrioid adenocarcinoma. Virchows Arch 454: 525-529.

[35] Koga K, Osuga Y, Tsutsumi O, Okagaki R, Momoeda M, et al. (2000) Increased concentrations of soluble tumour necrosis factor receptor (STNFR) I and II in peritoneal fluid from women with endometriosis. Mol Hum Reprod 6: 929–933.

[36] Khan KN, Masuzaki H, Fujishita A, Kitajima M, Sekine I, et al. (2003) Immunoexpression of hepatocyte growth factor and c-Met receptor in the eutopic endometrium predicts the activity of ectopic endometrium. Fertil Steril 79: 173–181.

[37] Prefumo F, Venturini PL, Fulcheri E. (2003) Analysis of p53 and c-erbB-2 expression in ovarian endometrioid carcinomas arising in endometriosis. Int J Gynecol Pathol 22: 83-88.

[38] Philippoussis F, Gagné D, Hugo P, Gosselin D (2004) Concentrations of alpha-fetoprotein, insulin-like growth factor binding protein-3, c-erbb-2, and epidermal growth factor in serum of patients with endometriosis. J Soc Gynecol Investig 11: 175–181.

[39] Aghajanova L, Tatsumi K, Horcajadas JA, Zamah AM, Esteban FJ, et al. (2011) Unique transcriptome, pathways, and networks in the human endometrial fibroblast response to progesterone in endometriosis. Biol Reprod 84: 801–815.

[40] Chung HW, Lee JY, Moon HS, Hur SE, Park MH, et al. (2002) Matrix metalloproteinase-2, membranous type 1 matrix metalloproteinase, and tissue inhibitor of metalloproteinase-2 expression in ectopic and eutopic endometrium. Fertil Steril 78: 787–795.

[41] Huang HF, Hong LH, Tan Y, Sheng JZ (2004) Matrix metalloproteinase 2 is associated with changes in steroid hormones in the sera and peritoneal fluid of patients with endometriosis. Fertil Steril 81: 1235–1239.

[42] Ramon L, Gilabert-Estelles J, Castello R, Gilabert J, Espana F, et al. (2005) mRNA analysis of several components of the plasminogen activator and matrix metalloproteinase systems in endometriosis using a real-time quantitative RT-PCR assay. Hum Reprod 20: 272–278.

[43] Bruner-Tran KL, Eisenberg E, Yeaman GR, Anderson TA, McBean J, et al. (2002) Steroid and cytokine regulation of matrix metalloproteinase expression in endometriosis and the establishment of experimental endometriosis in nude mice. J Clin Endocrinol Metab 87: 4782–4791.

[44] Saito T, Mizumoto H, Kuroki K, Fujii M, Mori S, et al. (1995) Expression of MMP-3 and TIMP-1 in the endometriosis and the influence of danazol. Nippon Sanka Fujinka Gakkai Zasshi 47: 495–496.

[45] Shan K, Lian-Fu Z, Hui D, Wei G, Na W, et al. (2006) Polymorphisms in the promoter regions of the matrix metalloproteinases-7,-9 and the risk of endometriosis and adenomyosis in China. Mol Hum Reprod 12: 35–39.

[46] Chung HW, Wen Y, Chun SH, Nezhat C, Woo BH, et al. (2001) Matrix metalloproteinase-9 and tissue inhibitor of metalloproteinase-3 mRNA expression in ectopic and eutopic endometrium in women with endometriosis: a rationale for endometriotic invasiveness. Fertil Steril 75: 152–159.

[47] Collette T, Maheux R, Mailloux J, Akoum A (2006) Increased expression of matrix metalloproteinase-9 in the eutopic endometrial tissue of women with endometriosis. Hum Reprod 21: 3059–3067.

[48] Szamatowicz J, Laudański P, Tomaszewska I (2002) Matrix metalloproteinase-9 and tissue inhibitor of matrix metalloproteinase-1: a possible role in the pathogenesis of endometriosis. Hum Reprod 17: 284–288.

[49] Sharpe-Timms KL, Keisler LW, McIntush EW, Keisler DH (1998) Tissue inhibitor of metalloproteinase-1 concentrations are attenuated in peritoneal fluid and sera of women with endometriosis and restored in sera by gonadotropin-releasing hormone agonist therapy. Fertil Steril 69: 1128–1134.

[50] Gottschal C, Malberg K, Arndt M, Schmitt J, Roessner A, et al. (2000) Matrix metalloproteinases and tace play a role in the pathogenesis of endometriosis. Adv Exp Med Biol 477:483–486.

[51] Finas D, Huszar M, Agic A, Dogan S, Kiefel H, et al. (2008) L1 cell adhesion molecule (L1CAM) as a pathogenetic factor in endometriosis. Hum Reprod 23: 1053–1062.

[52] Miller MA, Barkal L, Jeng K, Herrlich A, Moss M, et al. (2011) Proteolytic Activity Matrix Analysis (PrAMA) for simultaneous determination of multiple protease activities. Integr Biol (Camb) 3:422-438.

[53] Chen CH, Miller MA, Sarkar A, Beste MT, Isaacson KB, Lauffenburger DA, Griffith LG, Han J. (2012) Multiplexed Protease Activity Assay for Low-Volume Clinical Samples Using Droplet-Based Microfluidics and Its Application to Endometriosis. J Am Chem Soc 135: 1645–1648.

[54] Herrlich A, Klinman E, Fu J, Sadegh C, Lodish H (2008) Ectodomain cleavage of the EGF ligands HB-EGF, neuregulin1-beta, and TGF-alpha is specifically triggered by different stimuli and involves different PKC isoenzymes. FASEB J 22: 4281–4295.

[55] Storey, JD. (2002) A direct approach to false discovery rates. J Roy Stat Soc B 64:479–498.

[56] Brown CL, Meise KS, Plowman GD, Coffey RJ, Dempsey PJ (1998) Cell surface ectodomain cleavage of human amphiregulin precursor is sensitive to a metalloprotease inhibitor. Release of a predominant N-glycosylated 43-kDa soluble form. J Biol Chem 273: 17258–17268.

[57] Xu P, Liu J, Sakaki-Yumoto M, Derynck R (2012) TACE activation by MAPK-mediated regulation of cell surface dimerization and TIMP3 association. Sci Signal. 5: ra34.

[58] Canis M, Donnez JG, Guzick DS, Halme JK, Rock JA, et al. (1997) Revised American Society for Reproductive Medicine classification of endometriosis: 1996. Fertil Steril 67:817–821.

[59] Osteen KG, Hill GA, Hargrove JT, Gorstein F (1989) Development of a method to isolate and culture highly purified populations of stromal and epithelial cells from human endometrial biopsy specimens. Fertil Steril 52:965–972.

[60] Meyer AS, Hughes-Alford SK, Kay JE, Castillo A, Wells A, et al. (2012) 2D protrusion but not motility predicts growth factor-induced cancer cell migration in 3D collagen. J Cell Biol 197:721–729.

[61] Kim HD, Guo TW, Wu AP, Wells A, Gertler FB, Lauffenburger DA (2008) Epidermal growth factor-induced enhancement of glioblastoma cell migration in 3D arises from an intrinsic increase in speed but an extrinsic matrix- and proteolysis-dependent increase in persistence. Mol Biol Cell 19:4249–4259.

[62] Santella A, Du Z, Nowotschin S, Hadjantonakis AK, Bao Z (2010) A hybrid blob-slice model for accurate and efficient detection of fluorescence labeled nuclei in 3D. BMC Bioinformatics 11:580.

[63] Efron B, Gong G (1983) A leisurely look at the bootstrap, the jackknife, and cross-validation. Am Stat 37: 36–48.

[64] Höskuldsson A (1988) PLS regression methods. J Chemometr 2: 211–228.